The Astrophysical Journal, 823:85 (22pp), 2016 June 1 doi:10.3847/0004-637X/823/2/85

THE VIRUS-P EXPLORATION OF NEARBY GALAXIES (VENGA): RADIAL GAS INFLOW AND SHOCK EXCITATION IN NGC 1042

Rongxin Luo(罗荣欣)[1,2], Lei Hao[1], Guillermo A. Blanc[3,4,5], Shardha Jogee[6], Remco C. E. van den Bosch[7], and Tim Weinzirl[8]
[1] Key Laboratory for Research in Galaxies and Cosmology, Shanghai Astronomical Observatory, Nandan Road 80, Shanghai, 200030, China; haol@shao.ac.cn
[2] Graduate School of the Chinese Academy of Sciences, 19A, Yuquan Road, Beijing, China
[3] Departamento de Astronomía, Universidad de Chile, Camino del Observatorio 1515, Las Condes, Santiago, Chile
[4] Centro de Astrofísica y Tecnologías Afines (CATA), Camino del Observatorio 1515, Las Condes, Santiago, Chile
[5] Visiting Astronomer, Observatories of the Carnegie Institution for Science, 813 Santa Barbara Street, Pasadena, CA 91101, USA
[6] Department of Astronomy, University of Texas at Austin, 2515 Speedway, Stop C1400, Austin, TX 78712-1205, USA
[7] Max-Planck-Institut für Astronomie, Königstuhl 17, D-69117 Heidelberg, Germany
[8] School of Physics and Astronomy, The University of Nottingham, University Park, Nottingham, NG7 2RD, UK
Received 2015 July 25; accepted 2016 March 22; published 2016 May 25

ABSTRACT

NGC 1042 is a late-type bulgeless disk galaxy that hosts low-luminosity active galactic nuclei (AGNs) coincident with a massive nuclear star cluster. In this paper, we present the integral field spectroscopy studies of this galaxy, based on the data obtained with the Mitchell spectrograph on the 2.7 m Harlan J. Smith telescope. In the central 100–300 pc region of NGC 1042, we find a circumnuclear ring structure of gas with enhanced ionization, which we suggest is mainly induced by shocks. Combining this with the harmonic decomposition analysis of the velocity field of the ionized gas, we propose that the shocked gas is the result of gas inflow driven by the inner spiral arms. The inflow velocity is $\sim 32 \pm 10$ km s^{-1}, and the estimated mass-inflow rate is $\sim 1.1 \pm 0.3 \times 10^{-3}\ M_{\odot}$ yr^{-1}. The mass-inflow rate is about one hundred times the black hole's mass-accretion rate ($\sim 1.4 \times 10^{-5}\ M_{\odot}$ yr^{-1}) and slightly larger than the star-formation rate in the nuclear star cluster ($7.94 \times 10^{-4}\ M_{\odot}$ yr^{-1}), implying that the inflow material is enough to feed both the AGN activity and star formation in the nuclear star cluster. Our study highlights that secular evolution can be important in late-type unbarred galaxies like NGC 1042.

Key words: galaxies: active – galaxies: individual (NGC 1042) – galaxies: ISM – galaxies: kinematics and dynamics – galaxies: nuclei – ISM: kinematics and dynamics

1. INTRODUCTION

1.1. Feeding of Low-luminosity Active Galactic Nuclei

Since the discovery of the tight correlation between the masses of supermassive black holes (SMBHs) and the global properties of their host galaxies (Ferrarese et al. 2000; Gebhardt et al. 2000; Tremaine et al. 2002), the coevolution of galaxies and SMBHs has become an important topic in the study of galaxy formation and evolution. One outstanding problem is understanding how the host galaxy can feed the central black hole and trigger the nuclear activity. Theoretically, galaxies can affect the growth of black holes via global interaction processes, such as major or minor mergers, galaxy interactions, and gas accretions (Negroponte & White 1983; Sanders et al. 1988; Barnes & Hernquist 1991; Quinn et al. 1993; Mihos & Hernquist 1996; Kauffmann & Haehnelt 2000; Di Matteo et al. 2005; Hopkins et al. 2006, 2008). The galaxy-wide secular processes driven by a series of internal nonaxisymmetric structures (e.g., large-scale bars, spiral arms, ovals, nuclear spiral arms, and nested bars) can also play important roles in the growth of black holes (Jogee et al. 2002, 2005; Kormendy & Kennicutt 2004; Athanassoula 2008; Sellwood 2014 and references therein). These processes have been proposed to effectively dissipate the angular momentum and transfer material inward to the central regions of galaxies (Shlosman et al. 1989, 1990; Martini et al. 2004; Jogee 2006, and references therein).

Observationally, there have been many statistical studies to investigate the role of different feeding mechanisms. Studies of the links between nuclear activity and merger signatures (e.g., close pairs or disturbed hosts) have shown that major mergers have a limited role in triggering nuclear activities (Schawinski et al. 2010, 2011, 2012; Cisternas et al. 2011; Weinzirl et al. 2011; Kocevski et al. 2012; Simmons et al. 2012, 2013; Karouzos et al. 2014; Villforth et al. 2014) and may only dominate the feeding processes of the most luminous active galactic nuclei (AGNs; Kartaltepe et al. 2010; Koss et al. 2011; Rosario et al. 2012; Treister et al. 2012). The role of secular processes has been mainly tested by exploring the bar–AGN connection, which presents only marginal evidence for a direct correlation (Ho et al. 1997; Mulchaey & Regan 1997; Hunt & Malkan 1999; Shlosman et al. 2000; Laine et al. 2002; Laurikainen et al. 2004a; Lee et al. 2012; Oh et al. 2012; Cisternas et al. 2013, 2015; Cheung et al. 2015; Galloway et al. 2015). In addition, the dominant feeding mechanisms for AGNs of different luminosities and within different environments may be different (Jogee 2006; Kormendy & Ho 2013).

Another way to explore the feeding mechanisms of AGNs is to study the detailed properties of the interstellar medium (ISM) in the vicinity of the SMBHs. *Hubble Space Telescope* (*HST*) imaging has revealed various dust structures around AGNs, which are thought to be possible feeding channels of nuclear activity (Malkan et al. 1998). However, further studies on matched samples of active and inactive galaxies do not find a significant correlation between the circumnuclear dust and the nuclear activities (Martini et al. 2003), although there is an exception for the early-type AGN hosts (Simões Lopes et al. 2007).

With the advances in integral field spectroscopy (IFS), gas inflows have been directly observed from the two-dimensional

gaseous velocity field for more and more nearby AGNs (Fathi et al. 2006; Storchi-Bergmann et al. 2007; Riffel et al. 2008; Davies et al. 2009; Müller Sánchez et al. 2009; van de Ven & Fathi 2010; Riffel & Storchi-Bergmann 2011; Schnorr Müller et al. 2011; Riffel et al. 2013; Schnorr-Müller et al. 2014; Schönell et al. 2014). These detailed studies of individual sources have shown that the inflowing material could be multiphased, with typical inflow velocities of 50–100 km s^{-1} and a large range in mass-inflow rates (0.01–1 $M_\odot$ yr^{-1}). While IFS observations mainly probe the ionized and warm molecular phase of the ISM, the gas inflows have also been detected in the cold molecular phase with the observations of millimeter/submillimeter interferometry (García-Burillo & Combes 2012; Fathi et al. 2013; Combes et al. 2014). Furthermore, hints of kinematic differences have been observed in the local Seyfert galaxies. Dumas et al. (2007) found that the kinematics of the ionized gas in the circumnuclear regions of Seyfert galaxies show stronger perturbations than those in inactive galaxies. Hicks et al. (2013) reported that Seyfert galaxies have more concentrated stellar and H_2 surface brightness, lower stellar velocity dispersion, and elevated H_2 luminosity within ~100–200 pc compared to inactive galaxies. Davies et al. (2014) further showed that the circumnuclear disks of molecular gas widely exist in Seyfert galaxies. In these disks, the gas presents inflow and outflow kinematics superimposed on the disk rotations.

In this paper, we explore the feeding mechanism of the low-luminosity AGN (LLAGN) NGC 1042, based on the IFS data taken from the VENGA survey (VIRUS-P Exploration of Nearby Galaxies) (Blanc et al. 2013). We are interested in this object because it is a late-type bulgeless galaxy with an accreting intermediate-mass black hole (Shields et al. 2008). In recent years, LLAGNs have been found in the pesudobulges of late-type galaxies and even in the bulgeless/dwarf galaxies (Ho 2008; Greene 2012; Kormendy & Ho 2013, and references therein). These black holes generally have low masses ranging from 10^4 $M_\odot$ to 10^6 $M_\odot$ (Greene & Ho 2004, 2007; Dong et al. 2012; Reines et al. 2013). The scaling relations between these black holes and their host galaxies are less certain and may show much larger scatters than those of SMBHs in the classical bulges and ellipticals (Hu 2008; Greene et al. 2010; Kormendy et al. 2011; Sani et al. 2011; Kormendy & Ho 2013; McConnell & Ma 2013). This suggests their mass growth may not significantly correlate with the global processes in the hosts. Here, we use NGC 1042 as an example to study the mass growth of black holes at the low-mass end.

The paper is organized as follows. First, we describe the relevant properties of NGC 1042 in Section 1.2. In Section 2 we describe the observations and the data reduction. In Section 3, we present the two-dimensional (2D) maps of emission-line fluxes, emission-line ratios, the velocity field, and the velocity dispersions of ionized gas and stars in NGC 1042. We find a circumnuclear ring-like structure of ionized gas in the 100–300 pc region that shows LINER-like emission. In Section 4, we characterize the nature of this structure and quantify the kinematic properties of the ionized gas. We propose that this structure is the result of the gas moving inward, driven by the inner spiral arms of NGC 1042. In Section 5, we calculate the mass-inflow rate of the ionized gas and discuss its implications for AGN feeding and star formation in the nuclear star cluster. We summarize in Section 6.

Table 1
General Parameters of NGC 1042

Parameters (Unit)	Value
α(J2000.0)[a]	02:40:23.967
δ(J2000.0)[a]	−08:26:00.76
Type[b]	SAB(rs)cd
i[a](deg)	38.7 ± 0.5
θ[a](deg)	114.0 ± 1
d_{25}[b](arcmin)	4.7 × 3.6
D[c](Mpc)	4.2 ± 0.7
pc/"	20
M_K[d]	−19.27 ± 0.36
μ_B[b]	23.27
N_P[e]	2

Notes.
[a] Coordinates, inclination (i), and position angle (θ) used in this paper. See Appendix B for details.
[b] Morphology Type, isophotal diameter (d_{25}), and effective B-band surface brightness (μ_B) taken from RC3 (de Vaucouleurs et al. 1991).
[c] Method to determine distance: HI 21cm Tully-Fisher (Tully et al. 2008).
[d] From Jarrett et al. (2000).
[e] The number of Mitchell spectrograph pointings covering the galaxy.

1.2. NGC 1042

NGC 1042 is a nearby late-type (morphological type SAB(rs)cd, de Vaucouleurs et al. 1991) bulgeless galaxy. The basic properties of this galaxy are listed in Table 1. The spiral arms in NGC 1042 are composed of two symmetric inner arms and multiple long and continuous outer arms, which are classified as AC 9 in the classification of spiral arms in Elmegreen & Elmegreen (1987). In the RC3 catalog (de Vaucouleurs et al. 1991), NGC 1042 is classified as a weakly barred (SAB) spiral galaxy. Marinova & Jogee (2007) performed ellipse fitting on the B- and H-band images of this galaxy and also classified it as a barred galaxy (with a deprojected bar ellipticity of 0.6 and bar semimajor axis 4.4 kpc in the H band). However, using a different approach of multicomponent (bulge, bar, disk) decomposition, Weinzirl et al. (2009) found that NGC 1042 is best fit with a bulge and disk only and reclassify it as unbarred. The unbarred classification is also proposed by some other works. Laurikainen & Salo (2002) and Laurikainen et al. (2004b) used Fourier techniques on the B-, J-, H-, and K-band images and classified it as an unbarred galaxy. Buta et al. (2005) decomposed the perturbation strengths of gravitational potential induced by the bar and the spiral arms and proposed that the contribution of the spiral arms is dominant. They point out that the inner spiral arms sharply curve toward to the central region and produce a bar-like structure in NGC 1042, which can be misidentified as a bar. Based on the potential-density phase-shift method, Buta & Zhang (2009) confirmed their previous unbarred classification. In the Carnegie-Irvine Galaxy Survey, Li et al. (2011) also classify NGC 1042 as an unbarred galaxy based on visual inspection, the geometric analysis, and the Fourier method.

The coincidence of a nuclear star cluster and an AGN has been found in NGC 1042. The nuclear star cluster was first identified by an isophotal analysis of the *HST* images (Böker et al. 2002). After a detailed structural analysis, Böker et al. (2004) found that the effective radius of the cluster is ~0.″02 (1.94 pc at their adopted distance of 18.2 Mpc). The dynamical

mass and stellar population of the cluster were also presented by Walcher et al. (2005, 2006) with the VLT UVES spectroscopy. The obtained dynamical mass of the cluster is $\sim 3 \times 10^6\ M_\odot$. The observed mean cluster age and metallicity are 10^4 Myr and $Z = 0.02$, respectively. There is a young stellar population with a stellar age of $\sim$10 Myr in the underlying old (>1 Gyr) population of stars. The mass of this young stellar component is $\sim 7.94 \times 10^3\ M_\odot$ (Walcher et al. 2006).

Based on the high-resolution optical spectrum done within the central $1'' \times 1''$ region, Shields et al. (2008) claimed that a low-luminosity AGN exists (classified as a LINER) that is coincident with the nuclear star cluster in NGC 1042. They found that the peak of the Hα flux has an offset ($\sim$0.″5) from the peak of the forbidden lines and the stellar continuum. They also found that the profile of the [N II]+Hα emission lines is unusual: the [N II] lines deviate from Gaussian profiles and present high-velocity wings extending to about $\pm$300 km s^{-1} from the line center. Additionally, the FWHM of the [N II] is observed to be larger than that of the Hα. They proposed that this unusual profile can be explained as the blended emission from an LLAGN and an offset H II region. The H II region dominates the Hα emission and produces the offset of the peak of the Hα flux. After removing the contamination from the adjacent H II region, they estimated the bolometric luminosity of the AGN to be $L_{\rm bol} \sim 8 \times 10^{39}$ erg s^{-1} using the Hα luminosity, and they use it to set a lower limit on the mass of the black hole ($M_{\rm BH} > 60\ M_\odot$). Walcher et al. (2005, 2006) found that the *M/L* of the nuclear star cluster from the dynamical estimation is smaller than that from the stellar population analysis. Considering that the *M/L* estimated from the stellar components does not include any contributions from the black hole, Shields et al. (2008) concluded that the mass of the black hole and the nuclear cluster should be of similar order. They used $3 \times 10^6\ M_\odot$ as the upper limit of the black hole mass of NGC 1042. In addition, they used the velocity dispersion of the nuclear stellar cluster and the M–σ relation to estimate the black hole mass, which is $4 \times 10^5\ M_\odot$, implying an intermediate-mass black hole.

Interestingly, the distance of NGC 1042 has dramatically different values in the literature, ranging from 4.2 Mpc (Tully et al. 2008) to 18.2 Mpc (Böker et al. 2002). There are mainly two independent methods to determine the distance of this galaxy. The first method is based on the heliocentric velocity and uses Hubble's law to calculate the redshift distance. The motion of the local universe is corrected in the calculation. This method depends on the selection of the H_0 value and the models of local motions. The redshift distance estimated by this method is found to be 16.7 Mpc by Tully (1988), 18.2 Mpc by Böker et al. (2002), and 13.2 Mpc by Theureau et al. (2007). The former two estimations only correct for the infall of the Galaxy to the Virgo cluster, while Theureau et al. (2007) made a full model of the peculiar velocity to the Galaxy within 80 Mpc. In addition, they also corrected the peculiar velocity of NGC 1042. The second method is to make use of the Tully–Fisher (TF) relation. This method is therefore independent from the redshift. Several earlier estimations using this method determined the distance of NGC 1042 at $\sim$8 Mpc (8.4 Mpc from Tully et al. 1992; 7.8 Mpc, 7.77 Mpc, and 7.94 Mpc from J-, H-, and K-band estimations, respectively, of Theureau et al. 2007), but a later estimation by Tully et al. (2008) places NGC 1042 at 4.2 Mpc. This work adopts the Tully–Fisher relation calibrated in Tully & Pierce (2000) and shifts slightly its zero point to be consistent with the results of the *HST* Cepheid Key Project (Freedman et al. 2001). Interestingly, we find that the distance estimated by this method is very sensitive to the inclination angle adopted for the galaxy. Tully et al. (2008) used the B-band photometry to determine the inclination angle to be $\sim$57°. If we use the inclination angle of 37° that is indicated by the 2MASS photometry and use the same method as Tully et al. (2008), we find the distance of NGC 1042 is $\sim$8 Mpc. If we use the kinematic inclination (38.°7) measured from the harmonic decomposition modeling (HDM) of this paper (see Appendix B of this paper), the obtained distance changes to $\sim$7.3 Mpc. Since the large scatter of the distance estimations of NGC 1042 may require further exploration, which is beyond the focus of this paper, we choose the estimation from the latest literature (Tully et al. 2008), adopting 4.2 Mpc as the distance of NGC 1042 in this paper. It is also the smallest distance estimation of all in the literature so far, so our analyses can be considered as a reference for others by simply scaling up. We remind the readers to be cautious on the big uncertainties of the distance estimation of NGC 1042.

2. OBSERVATIONS AND DATA REDUCTION

2.1. Observations

The observations of NGC 1042 were carried out as part of the VENGA survey (Blanc et al. 2013), which is a wide-field, optical (3600–6800 Å) IFS survey of 30 nearby spiral galaxies. It uses the Mitchell spectrograph (formerly known as VIRUS-P, Hill et al. 2008) on the 2.7 m Harlan J. Smith telescope to observe about 44,000 individual spectra across the disks of these objects. As a fiber-fed integral field unit (IFU), Mitchell consists of 246 fibers sampling a $1.'7 \times 1.'7$ field of view with a one-third filling factor. The diameter of each fiber is 200 μm, corresponding to 4.″24 on the sky. The VP1 grating was used in a blue and a red setup to cover the spectral range from 3600 to 6800 Å with a spectral resolution of 5 Å (FWHM).

Figure 1 shows the r-band SDSS image[9] of NGC 1042, overlaid with the area covered by the Mitchell observations. Two slightly offset pointings of the Mitchell are used to map this galaxy across a 3.5 kpc × 2.5 kpc area. For each pointing, three dithers are observed at relative positions $(\Delta\alpha, \Delta\delta) = (0.''0, 0.''0)$, $(-3.''6, -2.''0)$, and $(0.''0, -4.''0)$ from the origin, to fill the whole area of the Mitchell field of view. The observation of each dither is divided into several science frames with exposure times ranging from 20 to 30 minutes. The 5 minute off-source frames are observed between each science frame, which are used to perform sky subtraction. The calibration frames (bias, arc lamps, twilight flats, and spectrophotometric standard stars) are also observed in the same night. A detailed description of the VENGA observing strategy is presented in Blanc et al. (2013).

The observational details of NGC 1042 are summarized in Table 2. For each dither in each pointing, we list the total on-source exposure time, the number of science frames, the average seeing of the frames, and the mean atmospheric transparency. NGC 1042 was observed in five runs of the VENGA survey. Observing conditions were variable between different runs and within different nights during the same observing run, ranging from photometric to partly cloudy with average atmospheric transparency down to $\sim$60%. Seventeen

[9] We obtain the mosaic image from http://data.sdss3.org/mosaics

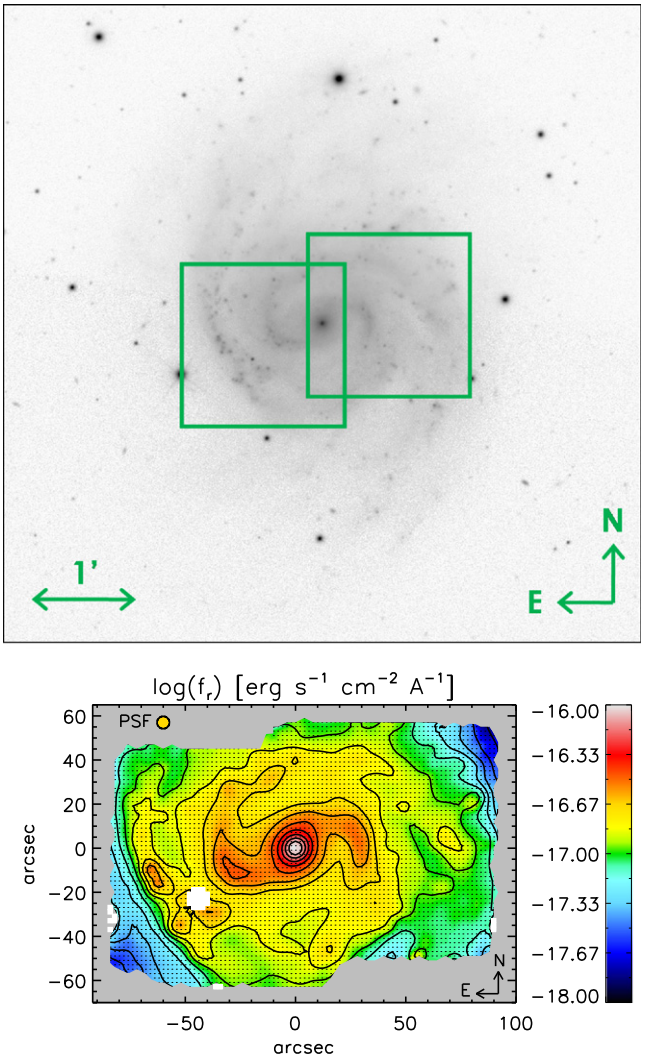

Figure 1. Top panel: the SDSS r-band image of NGC 1042. The green squares present two pointings of the Mitchell observations. Bottom panel: the reconstructed r-band flux map of NGC 1042. Black dots mark the position of each spaxel in the data cube. Black contours show isophotes of the SDSS r-band image. The foreground stars are masked as blank regions (see Section 2.2). The gold circle in the top left corner presents the 5.″6 FWHM PSF of the VENGA data.

out of 76 frames (22%) are rejected because of pointing errors or bad sky-subtraction problems. The seeing of the remaining good frames ranged from 1.″63 to 2.″93, with a median at 2.″20.

Overall we spent 27 hr of exposure time on the 59 good frames of this galaxy. As a result, the spectra have high signal-to-noise ratios (S/Ns) per spectral resolution element, with a median value at ∼100 in the continuum. In the central parts (500 pc × 500 pc) of the galaxy, we typically have S/N > 200, while the spectra in the outermost regions (from 2.0 to 2.5 kpc) have a median S/N ∼ 55. We only have 20 out of 4789 spaxels (0.42%) with S/N less than 10. They are mainly located at the right top corner of the galaxy, as shown in Figure 1.

2.2. Data Reduction

The details of the data processing and spectral analysis of the VENGA survey have been described in Blanc et al. (2013). As part of this survey, we reduce and analyze the data of NGC 1042 in the same way.

All raw data are reduced by the VACCINE pipeline (Adams et al. 2011; Blanc et al. 2013). VACCINE performs bias and overscan subtraction, flat fielding, cosmic-ray rejection, wavelength calibration, and sky subtraction. Then the frames of spectrophotometric standard stars are used to perform the relative flux calibration for the 2D spectra in each observing run. Afterward, the broadband images reconstructed from these 2D spectra are compared with the SDSS broadband images to perform the absolute flux calibration and astrometry. The flux errors are obtained by combining the read noises and Poisson uncertainties in the CCD processing and then propagated throughout the rest of the data reduction. The instrumental spectral resolution is measured from the emission lines in the arc lamp frames and fitted as a function of wavelength. All of this information is combined to generate a data cube and a row-stacked spectra (RSS) file of NGC 1042.

In these data sets, the spectra are resampled to a common wavelength grid at 1.1 Å for regularly linear sampling and $(\Delta\lambda/\lambda)\ c = 60\ \mathrm{km\ s^{-1}}$ for regularly logarithmic sampling. The spaxel has a regular scale of 2″ × 2″, which can roughly Nyquist-sample the final spatial point-spread function (PSF). For each spaxel, the final spectrum is obtained by combining the spectra of surrounding fibers using a Gaussian spatial filter and adopting an inverse variance weighting scheme. The FWHM of the Gaussian filter is 4.″24, matching the fiber size. The final spatial PSF is obtained by convolving the top-hat profile of the fiber (4.″24 diameter) with the seeing (∼2.″20) and the Gaussian filter (4.″24 FWHM). This PSF can be well described as a Gaussian with 5.″6 FWHM. At the distance of 4.2 Mpc for NGC 1042, it corresponds to 112 pc. For a detailed description of the data-combining process and data format, see Section 4.7 of Blanc et al. (2013).

The spectral analyses are performed by the PARADA pipeline, which involves the pPXF (Cappellari & Emsellem 2004) and GANDALF (Sarzi et al. 2006) software as the main fitting procedures. Before fitting the spectra, the Galactic extinctions are corrected by adopting a Milky Way extinction law as parameterized by Pei (1992) and the extinction values from the maps of Schlegel et al. (1998). The pPXF is used to fit the stellar continuum. The stellar line-of-sight (LOS) velocity (υ^*) and the velocity dispersion (σ^*) are estimated from the fit. The spectrum of each spaxel is fitted individually with a linear combination of stellar templates convolved with a LOS velocity dispersion (LOSVD) by using the "penalized pixel" technique (Cappellari & Emsellem 2004). The stellar templates are the same as those in Blanc et al. (2013). These templates are selected from MILES stellar library version 9.1 (Sánchez-Blázquez et al. 2006; Falcón-Barroso et al. 2011) and include 48 stars, which span a wide range in spectral types (O through M), luminosity classes (I through V), and metallicities ($-2 < [\mathrm{Fe/H}] < 1.5$). The spectral resolution of the templates and the observed spectra are matched to the worst instrumental resolution at any given wavelength in the data cube, which translates into a final spectral resolution of 110 km s^{-1} in the red setup and 200 km s^{-1} in the blue setup. The LOSVD can be parameterized by a Gauss–Hermite polynomial in pPXF, but we only fit for the first two moments υ^* and σ^*, which means that we actually fit a Gaussian LOSVD.

After constraining the stellar kinematics, we measure the emission-line properties with GANDALF. GANDALF fits the

Table 2
Summary of VENGA Observations of NGC 1042

Pointing	Equatorial Coord. α	δ	Setup	Dither	Exposure Time (hr)	N	⟨Seeing⟩ (″)	⟨Transparency⟩
			red	D1	2.00	4	2.20	0.87
P1	2:40:26.28	−8:26:07.70	red	D2	3.5	7	2.29	0.87
			red	D3	4	8	2.25	0.89
			blue	D1	0.83	2	2.00	0.71
			blue	D2	2.08	5	2.00	0.64
			blue	D3	1.67	4	2.00	0.73
			red	D1	2.06	6	2.20	0.65
P2	2:40:21.34	−8:25:56.10	red	D2	2.50	5	2.52	0.67
			red	D3	3.50	7	1.90	0.68
			blue	D1	2.08	5	2.58	0.68
			blue	D2	1.25	3	2.93	0.69
			blue	D3	1.25	3	1.63	0.65

full spectrum by recomputing the weights given to the different stellar templates and adding Gaussian profiles to model the emission lines. The stellar LOS velocity (v^*) and the velocity dispersion (σ^*) derived in the pPXF fitting are fixed in the GANDALF fitting. We tie the kinematics of all emission lines to a common set of parameters ($v_{\rm gas}$, $\sigma_{\rm gas}$) in order to improve the fitting quality of faint lines. This ensures that the kinematic parameters obtained are mostly constrained by the brightest emission lines in the spectrum (typically Hα, [O III]λ5007, and [O II]λ3727). The errors in emission-line parameters are estimated based on the covariance matrix computed during the nonlinear Levenberg–Marquardt fitting. In Table 3, we report the median S/N of each emission line over all spaxels in the data cube and the fraction of the observed area in which the emission lines are detected at 5σ and 3σ. We detect Hα at 5σ over 98% of the full data cube with a median S/N = 38.9. Most of the strong lines ([N II]$\lambda\lambda$6548, 6583, [S II]$\lambda\lambda$6717, 6731, Hβ, [O III]λ5007, [O II]$\lambda\lambda$3726, 3729 doublets) are detected at 3σ over more than ∼80% of the observed area.

We construct a series of 2D maps of NGC 1042, including the emission-line flux maps, the emission-line ratio maps, the maps of the velocity field, and the maps of the velocity dispersions. We identify the foreground Milky Way stars from the visual inspection of the stellar velocity field and the SDSS images. In all maps, we flag the spaxels contaminated by these stars and mask the surrounding spaxels within 5″ as blank regions. For the emission-line flux and ratio maps (Figures 2 and 5), we adopt a S/N cut of 5 for each line used in the corresponding maps to select the regions with reliable measurements. The spaxels that do not satisfy the above S/N cut are masked with blank regions. In the maps of the velocity field and the velocity dispersion of the ionized gas (Figure 7), the regions having a velocity error or a velocity dispersion error larger than 10 km s^{-1} are masked as blank regions.

3. RESULTS

3.1. Maps of the Emission-line Fluxes and the Line Ratios

Figure 2 presents maps of the emission-line fluxes of Hα, Hβ, [O II]λ3726+λ3729, [O III]λ5007, [N II]λ6584, and [S II] λ6716+λ6731 in NGC 1042. Figure 3 illustrates the errors corresponding to these flux measurements. The morphologies of the Balmer line strengths and the forbidden line strengths agree very well: all show clear spiral arms. The overall distribution of these emissions is significantly asymmetric. The emission in the eastern arms is stronger than in the western arms, suggesting that the eastern arms contain more active star-forming regions. In the inter-arm regions we can detect significant amounts of emission, with a surface brightness that is one to two orders of magnitude fainter than that in the arms. There is also an enhanced emission in the center.

The amount of dust reddening can be determined by comparing the observed Hα/Hβ ratio with the intrinsic Hα/Hβ ratio expected from the recombination theory. We assume an intrinsic Hα/Hβ ratio of 2.87 (Osterbrock & Ferland 2006) and a Milky Way extinction law as parameterized by Pei (1992). Figure 4 presents the map of $E(B-V)$ and the extinction-corrected Hα flux. The measured errors of $E(B-V)$ are obtained by propagating the uncertainties in the Hα and Hβ line

Table 3
Fitted Emission Lines in NGC 1042

Transition	Wavelength (Å)	Median S/N	Fraction-5σ	Fraction-3σ
[O II][a]	3726.03	9.7	0.84	0.94
[O II][a]	3728.73	…	…	…
[Ne III]	3868.69	1.4	0.02	0.07
[Ne III]	3967.40	0.5	<0.01	0.01
H8	3889.06	1.7	0.09	0.20
Hϵ	3970.08	1.7	0.08	0.18
Hδ	4101.73	2.3	0.18	0.34
Hγ	4340.47	5.3	0.52	0.77
[O III]	4363.15	0.9	<0.01	<0.01
HeII	4685.74	0.6	<0.01	0.01
Hβ	4861.32	16	0.91	0.95
[O III]	4958.83	2.8	0.23	0.42
[O III]	5006.77	8.6	0.78	0.90
[N I][a]	5197.90	1.3	<0.01	0.06
[N I][a]	5200.39	…	…	…
[N II]	6547.96	6.9	0.63	0.80
Hα	6562.80	38.9	0.98	0.99
[N II]	6583.34	21.2	0.94	0.97
[S II]	6716.31	13.3	0.93	0.96
[S II]	6730.68	9.2	0.83	0.94

Note.
[a] Since we cannot resolve the [O II]λ3727 and [N I]λ5200 doublets, we report the median S/N and fraction of the observed area in which the lines are significantly detected for the sum of the two doublet components.

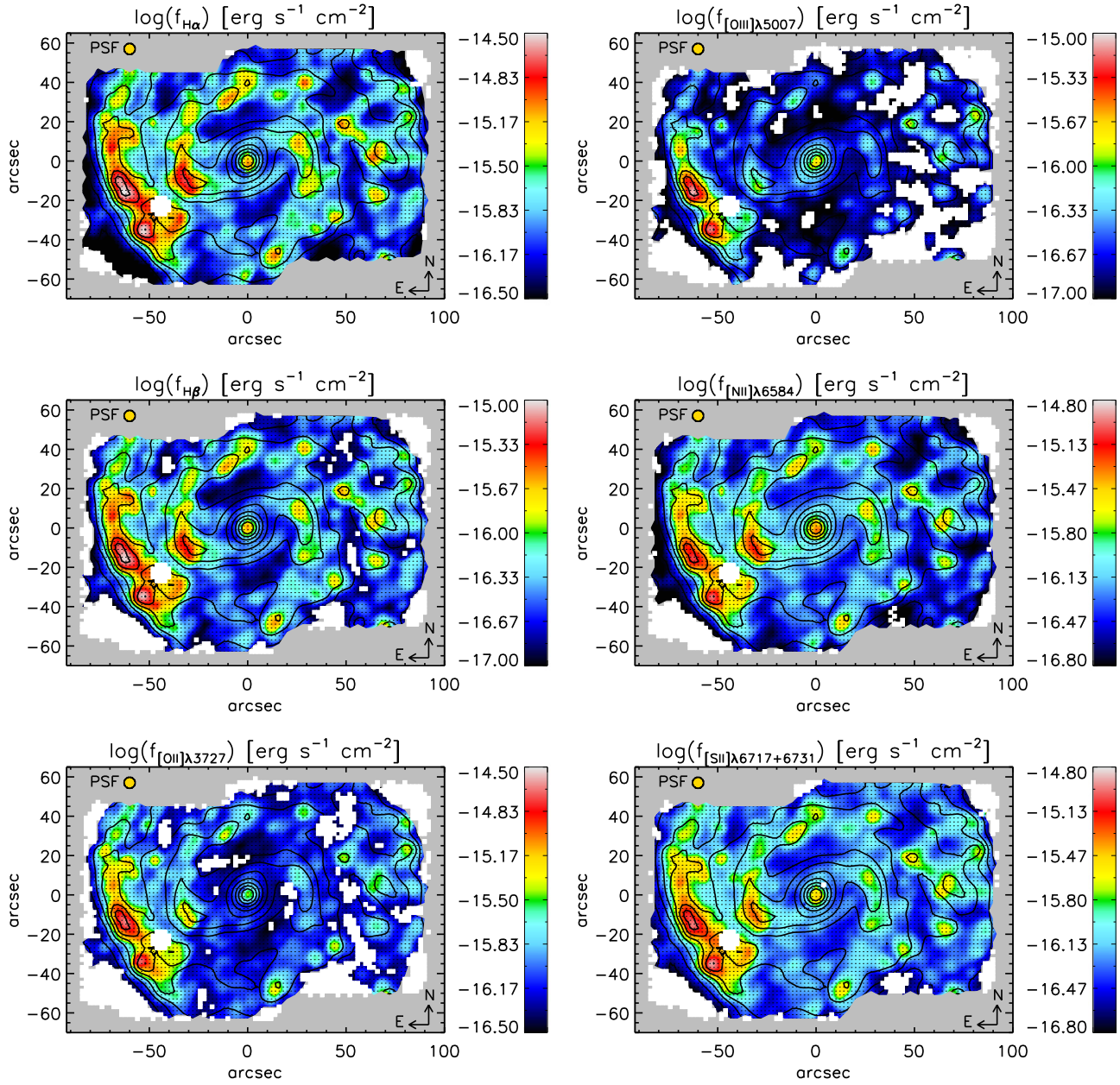

Figure 2. Emission-line flux maps of Hα, Hβ, [O II]λ3726+λ3729, [O III]λ5007, [N II]λ6584, and [S II]λ6716+λ6731 in NGC 1042. The spaxels contaminated by the foreground stars (see Section 2.2) and having line S/N below 5 are masked as blank regions. The gold circles in the top left corners present the 5.″6 FWHM PSF of the VENGA data. The black contours represent the SDSS r-band isophotes.

fluxes. In Figure 4 we masked the spaxels with error of $E(B-V)$ larger than 0.2 mag, which roughly amounts to an uncertainty of $\sim$50% in the extinction correction factor at the wavelength of Hα. The median extinction of NGC 1042 is about $A_V = 0.72$ mag (assuming $R_V = A_V/E(B-V) = 3.1$). Considering many spaxels have large errors in $E(B-V)$ because of weak Hβ fluxes, we decided not to perform the extinction corrections for the analysis in the rest of the paper since we mainly focus on the emission-line ratios from now on. The effect of dust reddening will not significantly influence the values of the emission-line ratios we are interested in because the central wavelengths of these lines are relatively close.

Figure 5 presents the maps of [O III]λ5007/Hβ, [N II]λ6584/Hα, and [S II]λ6716+λ6731/Hα. The line ratios of [O III]λ5007/Hβ and [N II]λ6584/Hα are sensitive to the ionization state and metallicity of the ionized gas. The line ratio of [S II]λ6716+λ6731/Hα traces a combination of temperature, ionization state, and metallicity of the ionized gas (Blanc et al. 2015). The higher values of these line ratios mean a higher ionization state of the gas. The higher [O III]λ5007/Hβ, [N II]λ6584/Hα, and [S II]λ6716+λ6731/Hα are detected in the inter-arm regions, with $\sim$0.3 dex greater than those detected in the arms. This can be attributed to the existence of the diffuse ionized gas (DIG). The DIG is a layer of nearly fully ionized hydrogen around bright H II regions, which can extend to the inter-arm regions and several kiloparsecs above and below the midplane of disk galaxies (Mathis 2000; Blanc et al. 2009; Haffner et al. 2009). It has been considered as a major component of the ISM of the Milky Way and other disk galaxies (see reviews by Mathis 2000 and Haffner et al. 2009).

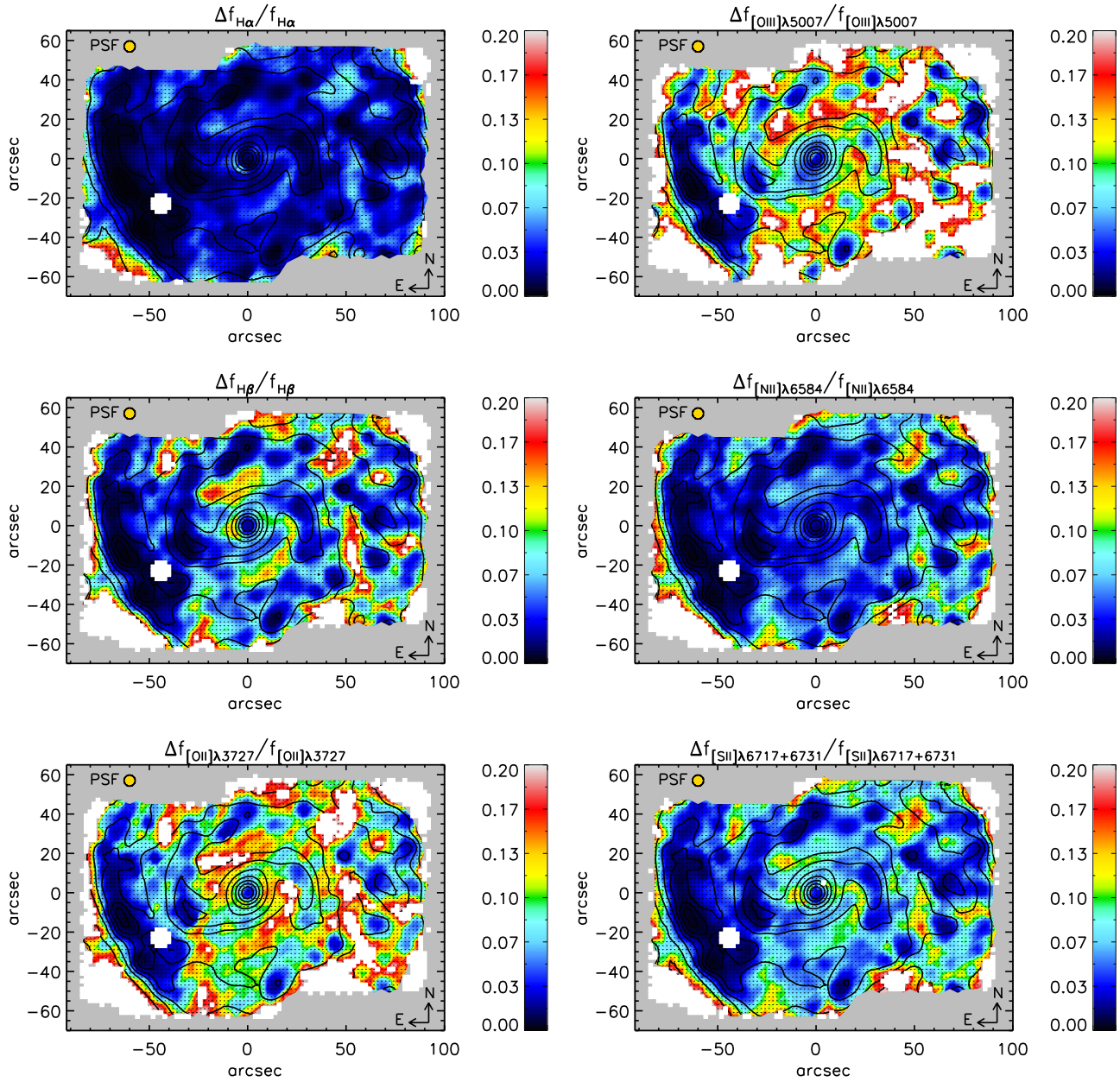

Figure 3. Error maps of the emission-line fluxes from Hα, Hβ, [O II]λ3726+λ3729, [O III]λ5007, [N II]λ6584, and [S II]λ6716+λ6731 in NGC 1042. The spaxels contaminated by the foreground stars (see Section 2.2) and having line S/N below 5 are masked as blank regions. The gold circles in the top left corners present the 5.″6 FWHM PSF of the VENGA data. The black contours represent the SDSS r-band isophotes.

The main ionization source of the DIG is the Lyman continuum photons leaking from the H II regions associated with the hot stars (Haffner et al. 2009, and references therein). In DIG, the detected Balmer and forbidden emissions are more diffused, and the observed line ratios of [O III]λ5007/Hβ, [N II]λ6584/Hα, and [S II]λ6716/Hα are always enhanced (Bland-Hawthorn et al. 1991; Haffner et al. 1999; Reynolds et al. 1999; Hoopes & Walterbos 2003; Madsen et al. 2006; Voges & Walterbos 2006, Kaplan et al. submitted).

In addition to the DIG component, we also find a circumnuclear ring-like ionized gas structure (CRIGS) that shows enhanced line ratios in the central region. We show the zoomed-in maps of the emission-line ratios in the central 500 pc × 500 pc region in Figure 6. This structure extends from 100 to 300 pc from the center. The values of [O III]λ5007/Hβ, [N II]λ6584/Hα, and [S II]λ6716+λ6731/Hα in the CRIGS are ∼0.5 dex higher than the typical values seen in the spiral arm and ∼0.2 dex higher than the typical values of DIG in the inter-arm regions. The enhanced [O III]λ5007/Hβ in this location has also been observed by the SAURON survey (Ganda et al. 2006). This ring structure is different from the well-known circumnuclear star-forming rings in some galaxies that are located at several hundreds of parsecs from the center (Comerón et al. 2010, 2014). These star-forming rings show enhanced star formation and thus enhanced Balmer emission-line fluxes compared to their disk regions. For the CRIGS in NGC 1042, neither Hα nor Hβ fluxes are enhanced. On the contrary, they show slight deficits. The [O III]λ5007, [N II]λ6584, and [S II]λ6716+λ6731 fluxes are also slightly weaker in the CRIGS, but the line ratios of [O III]λ5007/Hβ, [N II]λ6584/Hα, and [S II]λ6716+λ6731/Hα are enhanced compared to other regions of NGC 1042.

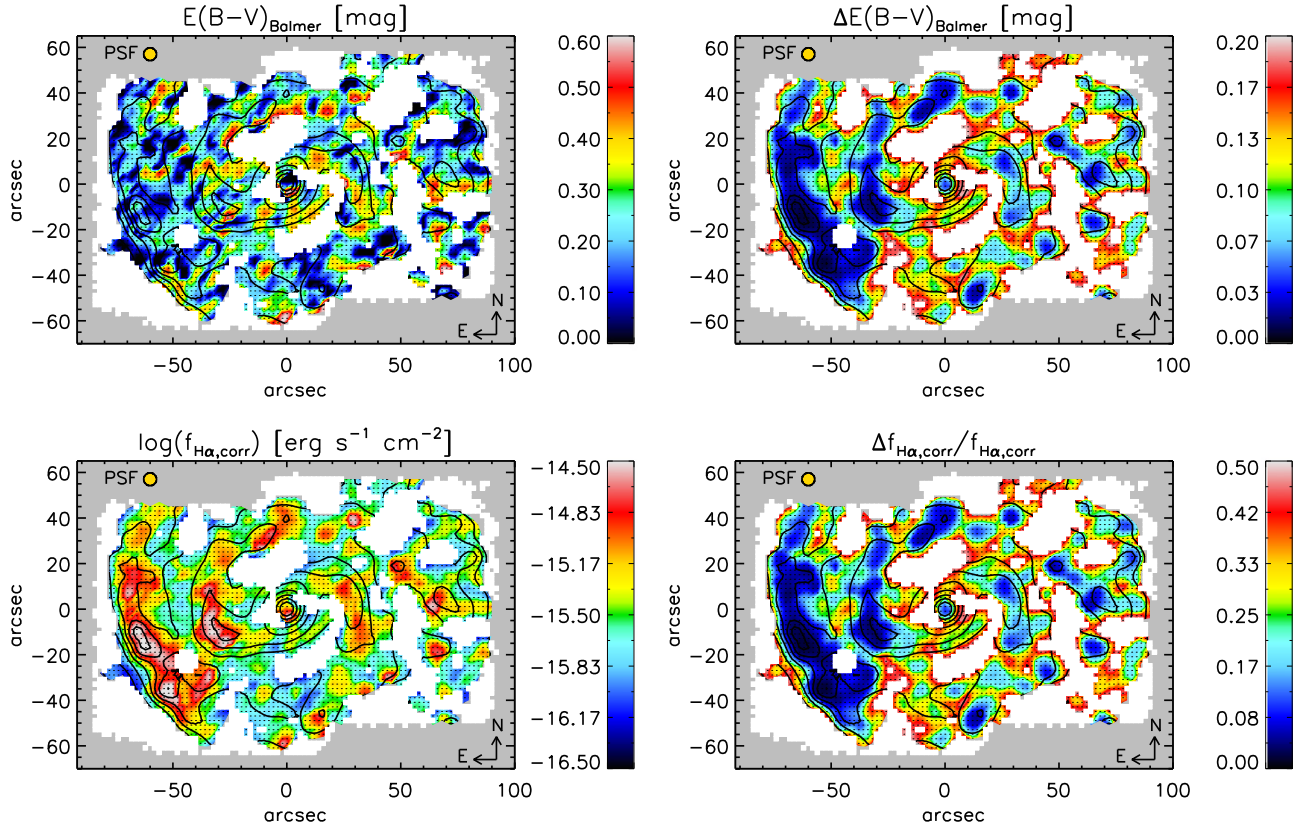

Figure 4. Top panel: map of dust reddening $E(B-V)$ and its error in NGC 1042. We masked the spaxels with error of $E(B-V)$ larger than 0.2 mag as blank regions, which roughly amounts to an uncertainty of ∼50% in the extinction correction factor at the wavelength of Hα. Bottom panel: map of extinction-corrected Hα fluxes and their relative errors in NGC 1042. In both maps, the spaxels contaminated by the foreground stars are also masked (see Section 2.2). The gold circles in the top left corners present the 5.″6 FWHM PSF of the VENGA data. The black contours represent the SDSS r-band isophotes.

3.2. Maps of the Velocity Field and the Velocity Dispersion of Ionized Gas

In Figure 7 we present the maps of the velocity field and the velocity dispersion of the ionized gas in NGC 1042. The error associated with the velocity is a combination of the errors in the emission-line measurements and in the wavelength calibrations. The errors for the velocity dispersion are obtained from the GANDALF fitting.

In addition to the map of the observed velocity dispersion, we also show the map of the intrinsic velocity dispersion of the ionized gas, which is obtained by subtracting the instrumental spectral resolution of the red setup (∼110 km s^{-1}, see Section 2.2) in quadrature from the observed velocity dispersion. Blanc et al. (2013) showed that the stellar velocity dispersion of the VENGA galaxies can be largely overestimated when the intrinsic velocity dispersion is significantly smaller than the instrumental resolution, using the Monte Carlo simulations. We do not perform a similar analysis on the velocity dispersion of the ionized gas, and it could also be overestimated for the regions with relatively low intrinsic velocity dispersion. However, for the regions with an intrinsic velocity dispersion comparable to or larger than the instrumental resolution, our measurements are robust.

In general, the ionized gas follows a regular circular rotation. Some extent of twists exists in the central 500 pc × 500 pc region. The velocity dispersion in the inter-arm region is relatively higher than that in the spiral arm, while some bright H II regions also show enhanced velocity dispersions. As shown in Figures 6(e) and (f), the ionized gas in the central 500 pc × 500 pc region presents a strongly spiral-like kinematic twist and a significant enhancement of velocity dispersion in the CRIGS, reaching to 90–130 km s^{-1}. This is higher than the typical values of the ionized gas in spiral galaxies (35 km s^{-1}, Epinat et al. 2008).

3.3. The LINER-like Emission in the CRIGS of NGC 1042

The "Baldwin, Phillips, and Terievich" (BPT) diagrams (Baldwin et al. 1981; Veilleux & Osterbrock 1987) of spectra in the central 500 pc × 500 pc region are shown in the top panel of Figure 8. We ignore the data points with emission lines in the corresponding diagram having S/N < 5. The data points are color coded with different galactocentric radii. In the bottom panel of Figure 8, we present the schematic maps of classifications based on the BPT diagrams. In the [O III]λ5007/Hβ versus [N II]λ6584/Hα diagram, regions with nebular emission dominated by the H II regions only lie at a galactocentric radius larger than 300 pc, while most regions within the 300 pc are located in the composite part. The regions associated with the CRIGS are mainly located at the LINER part. In the [O III]λ5007/Hβ versus [S II]λ6716+λ6731/Hα diagram, most regions are located in the star-forming part, although a large fraction of them are located in the composite part of the [O III]λ5007/Hβ versus [N II]λ6584/Hα diagram. The regions associated with the CRIGS are also located in the Seyfert/LINER region.

As shown in the classification schematic map, most regions in the CRIGS present LINER-like emission. In the rest of this paper, we aim to characterize the nature of this structure by

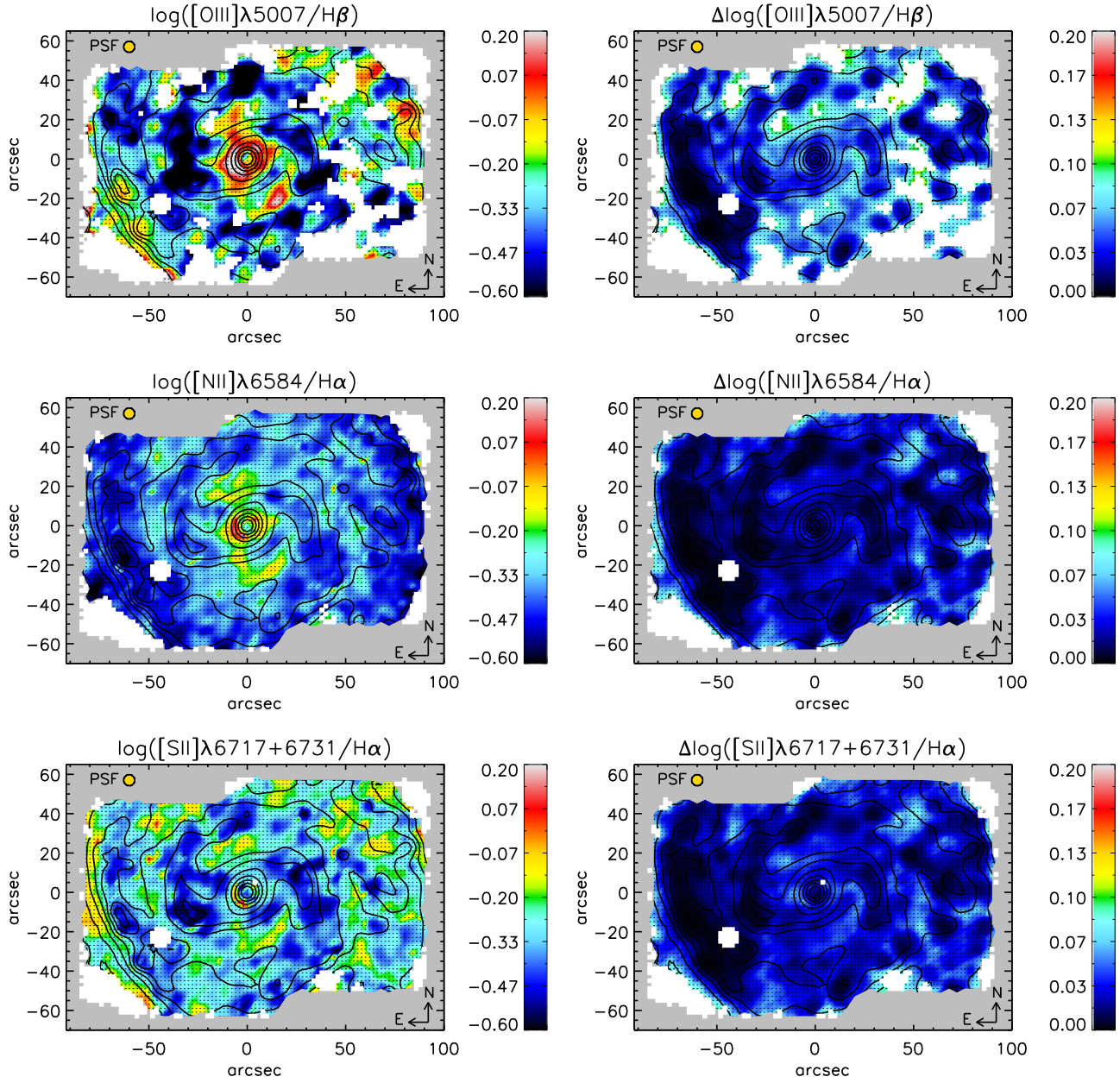

Figure 5. Error maps of the emission-line ratios, [O III]λ5007/Hβ, [N II]λ6584/Hα, and [S II]λ6716+λ6731/Hα in NGC 1042. In each map, the spaxels contaminated by the foreground stars are masked as blank regions (see Section 2.2). The spaxels are also masked as blank regions if any emission line used in each map has S/N < 5. The gold circles in the top left corners present the 5.″6 FWHM PSF of the VENGA data. The black contours represent the SDSS r-band isophotes.

analyzing the excitation mechanism of the LINER-like emission in Section 4.1 and by quantifying the kinematic properties of the ionized gas in Section 4.2 in the CRIGS.

4. ANALYSIS

4.1. Excitation Mechanism of the CRIGS in NGC 1042

Several ionization mechanisms can give rise to a LINER-like emission. The dominant mechanism can vary in different galaxies and even in different regions within the same galaxy. AGNs, post-asymptotic giant branch (p-AGB) stars, and shocks are the main candidates (Ho 2008). In this section, we discuss the dominant ionization mechanism of the CRIGS in NGC 1042.

4.1.1. Photoionization from the Central AGNs

Photoionization from the central AGNs has been considered as the most important ionization mechanism of the LINER-like emission in the central few hundred parsecs of galaxies (Ferland & Netzer 1983; Halpern & Steiner 1983; Pequignot 1984; Binette 1985; Ho et al. 1993; Groves et al. 2004). We investigate the role of this mechanism in the CRIGS through analyzing the distribution of the ionization parameter as a function of radius in the central 500 pc × 500 pc region of NGC 1042.

The dimensionless ionization parameter has been widely used to describe the ionization state of gas in galaxies. This parameter is defined as $U = Q/(n_e c)$, where Q is the flux density of the ionizing photons passing through the gas clouds,

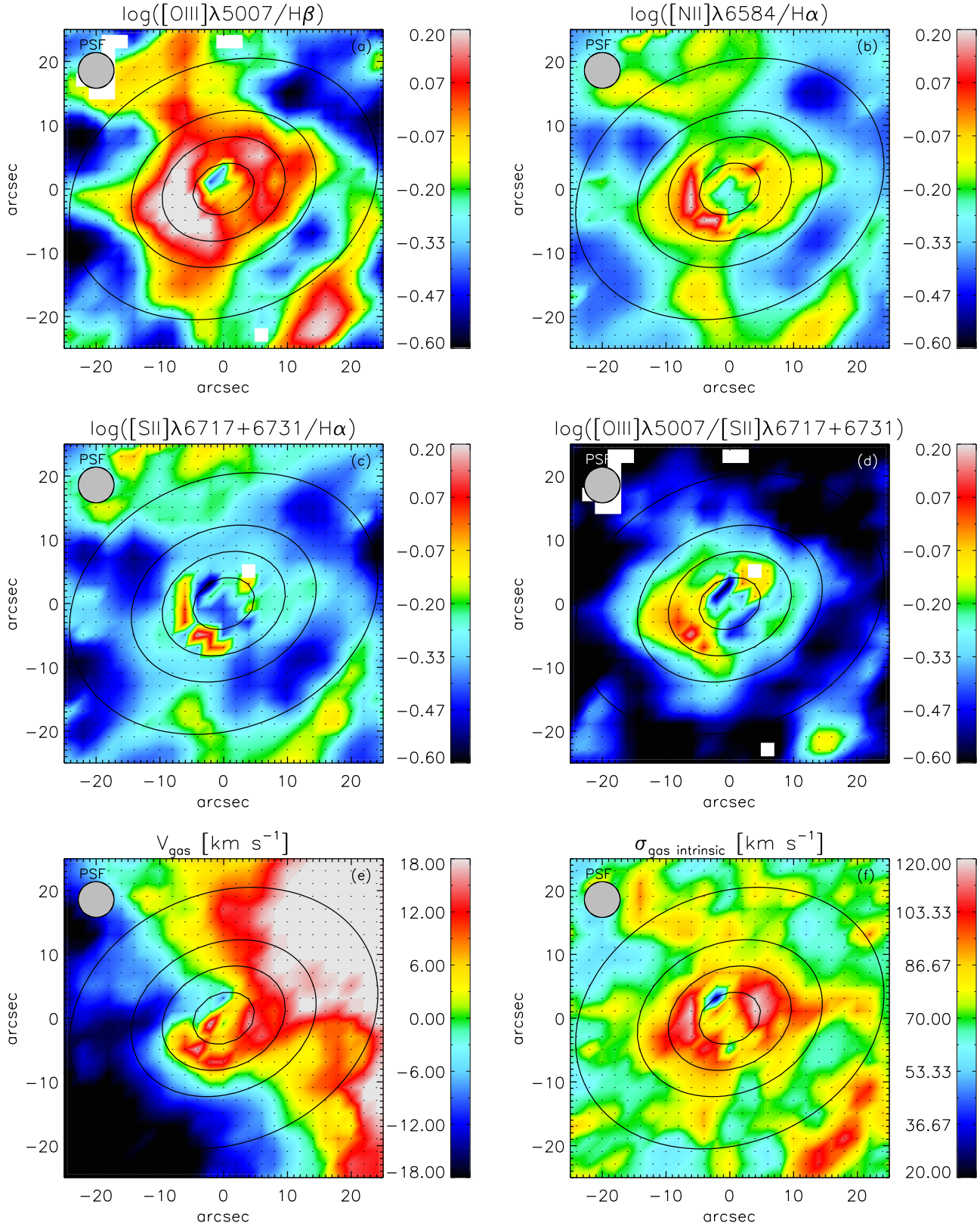

Figure 6. The zoomed-in maps of the emission-line ratios, the velocity field, and the velocity dispersion of the ionized gas in the central 500 pc × 500 pc of NGC 1042. The spaxels are masked as blank regions if any emission line used in each map has S/N < 5. The gray circles in the top left corners present the 5.″6 FWHM PSF of the VENGA data. The black contours represent the constant radii of 0.1, 0.2, 0.3, and 0.5 kpc.

n_e is the electric density of the ionized gas, and c is the speed of light. Because of the central ionizing property of AGNs, one can predict an r^2 dilution of Q around this ionization source. When combining with the observed n_e of the ionized gas, we can estimate the behavior of U as a function of radius if the gas is photoionized by AGNs.

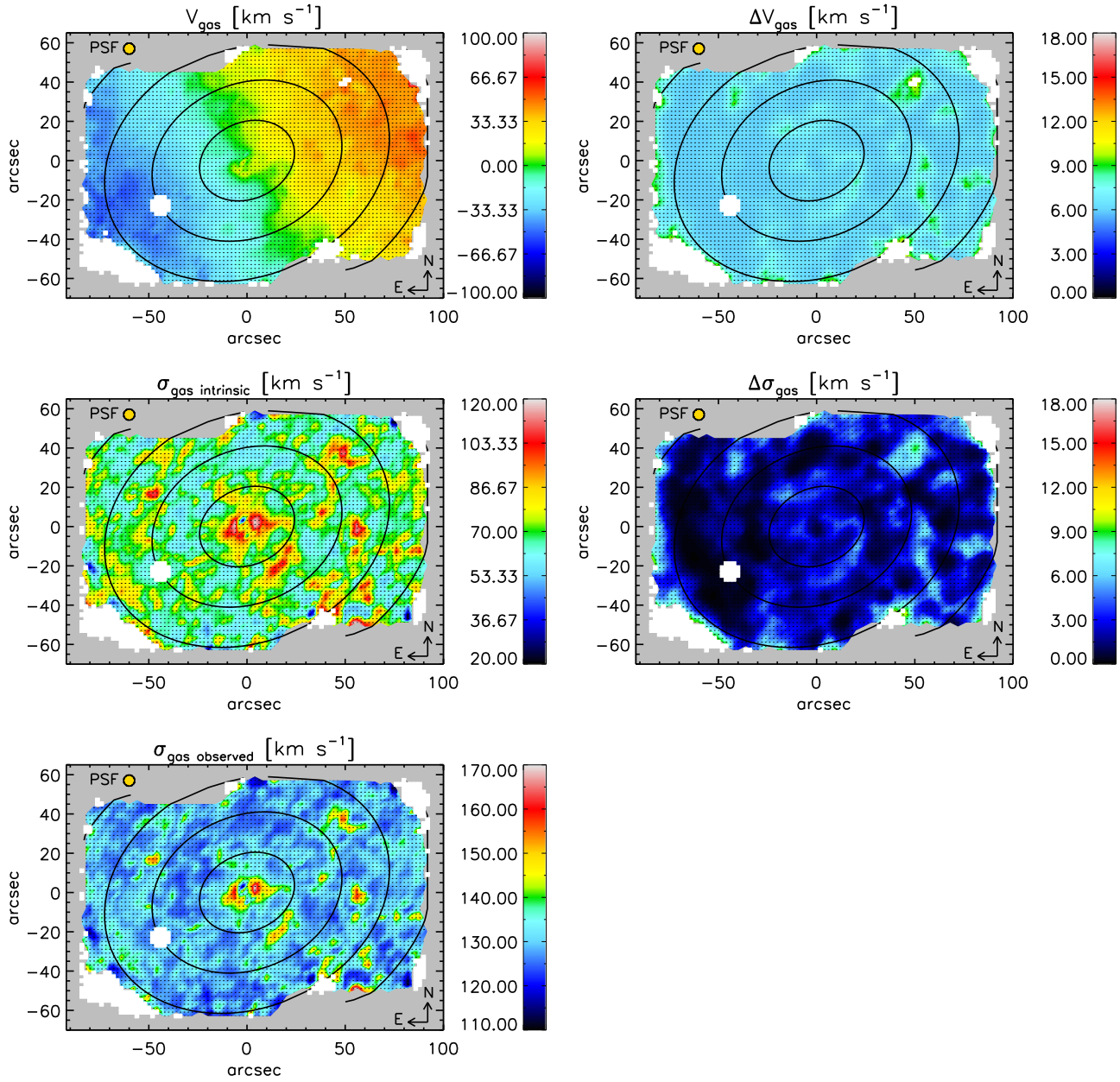

Figure 7. Maps of the velocity field and the velocity dispersion (both observed and intrinsic) of the ionized gas in NGC 1042 and their corresponding error maps. The spaxels contaminated by the foreground stars and having velocity error (or velocity dispersion error) larger than 10 km s^{-1} are masked. The gold circles in the top left corners present the 5.″6 FWHM PSF of the VENGA data. The black contours represent the constant radii in steps of 0.5 kpc.

Figure 9 shows the maps of [S II]λ6716/[S II]λ6731 and its error, and the radial profile of [S II]λ6716/[S II]λ6731 in the central 500 pc scale. The [S II]λ6716/[S II]λ6731 is a function of n_e and only weakly depends on the gas temperature. It has been widely used as an indicator for n_e. As shown in Figure 9, the line ratio of the [S II] doublets indicates a fairly constant n_e as a function of radius in the central 500 pc. Thus, if the clouds are photoionized by the central AGN, the predicted behavior of U in this region should in principle follow that of Q and also shows an r^2 dilution. This argument assumes a constant gas filling factor throughout the inner few hundred parsecs of the galaxy. An increased filling factor could result in a slope shallower than 2, but we should still expect a continuous decrease in U as a function of radius.

The observed distribution of U, which can be indicated by the [O III]λ5007/Hβ (Figure 6(a)), are inconsistent with this prediction. Based on the photoionization models, Yan & Blanton (2012) found that the [O III]λ5007/[S II]λ6716+6731 ratio can also be used to trace U. Thus, we also present in Figure 6(d) the map of the [O III]λ5007/[S II]λ6716+6731. This line ratio has characteristics similar to the [O III]λ5007/Hβ map, which shows an enhancement in the CRIGS $\sim$100–300 pc away from the nucleus. Therefore, from a morphological point of view, photoionization from the central AGN cannot be the mechanism of the observed LINER-like emission in the CRIGS.

4.1.2. Post-AGB Stars

Photoionization from post-AGB stars is another mechanism for the LINER-like emission in galaxies. These stars can produce a diffuse radiation field and provide sufficient ionizing photons

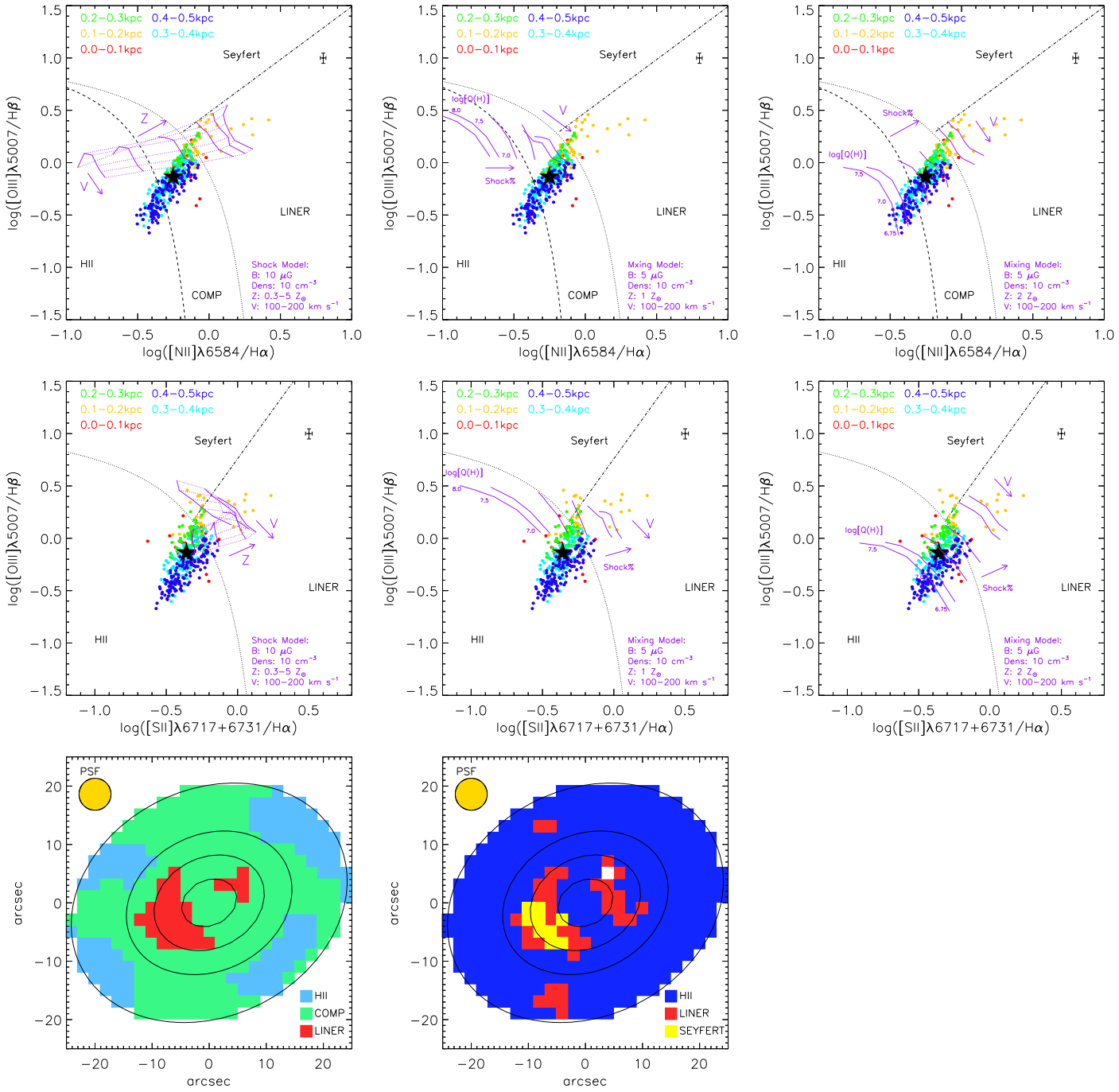

Figure 8. Top panel: BPT diagrams of spectra in the central 500 pc × 500 pc region. The dots represent the line ratios of different spaxels, and the colors reflect their galactocentric radii. The filled black stars show the integrated line ratios across this region. Dashed and dotted curves show the AGN/star-formation selection criteria of Kauffmann et al. (2003) and Kewley et al. (2001), respectively. The dash-dotted lines show the Seyfert/LINER demarcation of Cid Fernandes et al. (2010) and Kewley et al. (2006) in the [O III]λ5007/Hβ vs. [N II]λ6584/Hα diagram and the [O III]λ5007/Hβ vs. [S II]λ6716+λ6731/Hα diagram, respectively. The purple curves present the slow shock models from Rich et al. (2010, 2011). The detailed parameters of these models are introduced in Section 4.1.3. Bottom panel: schematic maps of the classifications based on the BPT diagrams.

to account for the extended LINER-like emission in galaxies (Binette et al. 1994; Stasińska et al. 2008; Sarzi et al. 2010; Cid Fernandes et al. 2011; Yan & Blanton 2012; Singh et al. 2013).

However, we do not think that the post-AGB stars are the dominant mechanism behind the observed nebular emission in the CRIGS. A post-AGB star is the final phase of the stellar evolution for stars with low and intermediate initial masses (van Winckel 2003). Therefore, the spatial distribution of post-AGB stars should follow that of the overall stellar distribution and present an extended smooth ionization field over the whole galaxy. This is inconsistent with the morphology of the CRIGS. In addition, as shown in Figure 10, the stars follow the regular circular rotation in the CRIGS, and the disturbed motion and enhanced velocity dispersion only appear in the gas. This suggests that the underlying ionization mechanism in the CRIGS is strongly connected with the gas, not with the stars.

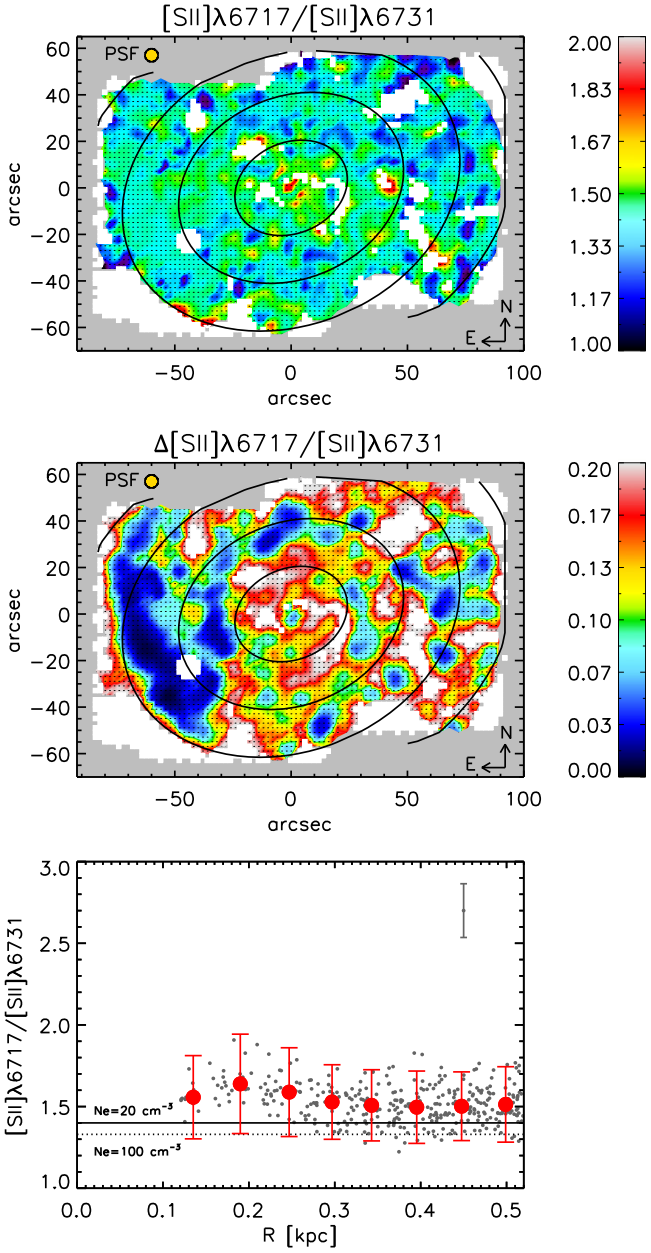

Figure 9. Top panel: emission-line ratio map of [S II]λ6716/[S II]λ6731 in NGC 1042. Middle panel: map of relative error of [S II]λ6716/[S II]λ6731 in NGC 1042. In these two figures, the spaxels contaminated by foreground stars and having line S/N below 5 are masked. The gold circles in the top left corners present the 5.″6 FWHM PSF of the VENGA data. The black contours represent the constant radii in steps of 0.5 kpc. Bottom panel: radial profile of the [S II] ratio in the central 500 pc scale. The spaxels having line S/N below 5 are not included. The [S II] ratios within the central 120 pc region are not shown because of the limit of the FWHM of the PSF (5.″6) in our observation. Gray dots present the value of the [S II] ratios in each spaxel. Gray error bars in the top right corner show the median error of the [S II] ratios. Red dots show the median of the [S II] ratios within the bin of 50 pc. The solid and dotted lines correspond to $n_e = 20$ cm^{-3} and 100 cm^{-3}, respectively.

4.1.3. Shock Excitation

Radiative shocks can also produce LINER-like emissions in galaxies. The collisional excitation in the postshock region radiates a large amount of photons and can generate LINER-like emission in galaxies. Shock-induced LINER-like emission has been observed in systems associated with galactic winds (Veilleux et al. 2003; Monreal-Ibero et al. 2006; Rich et al. 2010, 2011; Sharp & Bland-Hawthorn 2010; Kehrig et al. 2012; Arribas et al. 2014; Ho et al. 2014) and the intergalactic medium in clusters (Farage et al. 2010; McDonald et al. 2012).

We compare the observed properties of the ionized gas (line ratios and velocity dispersion) in the CRIGS with the predictions of the radiative shock models. The models of steady-flow radiative shocks have been developed by Sutherland & Dopita (1993) and Dopita & Sutherland (1995, 1996) and are summarized in Dopita & Sutherland (2003). In these models, the radiative fluxes and emission-line spectra of different shock components are calculated under four physical parameters: preshock density, shock velocity, magnetic parameter, and medium metallicity. The model-predicted flux ratios of different diagnostic lines and the corresponding shock velocities can be used to compare with the observed emission-line ratios and velocity dispersion of the gas. Of course, the shock-induced enhancement of gas velocity dispersion strongly depends on the shock geometry, and we do not expect a one-to-one match. But considering that the shocks can always accelerate the medium and the shock front cannot be fully resolved within the observed spatial resolution, some positive correlation between the shock velocity and the velocity dispersion of shocked gas is expected. This kind of correlation has indeed been observed in microquasar S26 (Dopita et al. 2012).

In the fast radiative shock models ($V_s >$ ~200 km s^{-1}), the ionizing photons from the postshock region will go through the preshock medium and generate a photoionization front (precursor) ahead of the shock front, which is also included in the calculation of the emission-line spectrum. In the slow radiative shock models ($V_s <$ ~200 km s^{-1}), the ionizing photons from the postshock region will be absorbed in the vicinity of the shock front. The radiation contribution of the photoionization precursor is negligible, and the detailed emission-line spectrum is more related to the shock itself. Since the velocity dispersion of the ionized gas in the CRIGS (90–130 km s^{-1}) is significantly lower than the typical velocities of the fast radiative shock models, we only compare our observations with the slow radiative shock models.

In recent years, a series of slow radiative shock models have been developed and used to test the shock excitation in different environments (Farage et al. 2010; Rich et al. 2010, 2011; McDonald et al. 2012; Ho et al. 2014). In Rich et al. (2010), the model grids are calculated for a fully preionized medium with cloud densities $n = 10$ cm^{-3}, metallicities $Z = 0.3$, 0.5, 1, 2, 3, and 5 $Z_\odot$, shock velocities ranging from 100 to 200 km s^{-1} (in steps of 20 km s^{-1}), and $B = 5$ μG. In Rich et al. (2011), the slow radiative shock model is combined with the photoionization model of H II regions to produce a mixing model, in which the line ratios vary with the fraction of the shock components. The model grids of the H II region are generated with varying ionization parameters and metallicities. For the model grids with $Z = 1$ $Z_\odot$ and 2 $Z_\odot$, log[$Q(H)$] is from 7.0 to 8.0 cm s^{-1} and from 6.75 to 7.5 cm s^{-1}, respectively.

We plot our observed BPT diagrams together with the models from Rich et al. (2010, 2011) in Figure 8. In general, these models can explain some of the data points in the CRIGS. The models in the [O III]λ5007/Hβ versus [S II]λ6716+λ6731/Hα diagram can provide a better match to the data points in the CRIGS than that in the [O III]λ5007/Hβ versus [N II]λ6584/

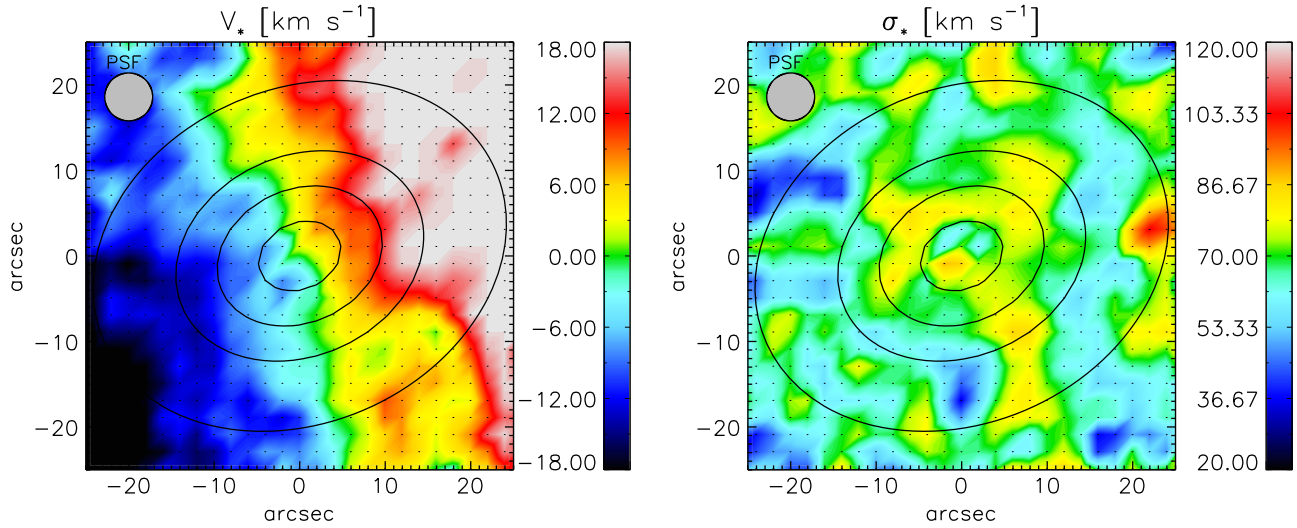

Figure 10. The zoomed-in maps of the velocity field and the velocity dispersion of the stars in the central 500 pc × 500 pc of NGC 1042. The gray circles in the top left corners present the 5.″6 FWHM PSF of the VENGA data. The black contours represent the constant radii of 0.1, 0.2, 0.3, and 0.5 kpc.

Hα diagram. In the mixing models, the grids with higher shock fractions can match the data better. The matched shock velocities in these models range from 100 to 180 km s^{-1}, which is roughly consistent with the velocity dispersion of the ionized gas in the CRIGS (90–130 km s^{-1}). Based on the above comparisons, we propose that the enhanced emission-line ratios and velocity dispersion in the CRIGS are related to the shock phenomenon.

4.2. Kinematic Analysis of the Ionized Gas

Radiative shocks are strongly related to the kinematic behavior of the ionized gas. Inflows induced by the nonasymmetric structures, outflows driven by starbursts or AGNs, and cloud collisions can produce shocks in the ISM. The kinetic energy of gas supersonic motions can be effectively dissipated through radiative shocks. In order to understand the kinematic properties of the ionized gas in the CRIGS, we compare the observed velocity field of the ionized gas with the velocity field model of a pure rotating disk.

We construct the velocity field model using the method of harmonic decomposition modeling (HDM). This method uses different Fourier components of the LOS velocity to describe the kinematic properties of galaxies and construct the corresponding velocity field models (a more detailed description of the HDM is in Appendix A). We use the IDL package Kinemetry (Krajnović et al. 2006) to perform the HDM. First, we determine the geometry parameters of the pure rotating disk and the system velocity of NGC 1042 (see Appendix B for details). Next, we fix these parameters and decompose the LOS velocity field into a series of Fourier components in a set of elliptical annuli along the semimajor axis of the galaxy. We expand the Fourier terms to the third order ($V_{\rm LOS}(R, \psi) = A_0(R) + \sum_{n=1}^{3}[A_n(R)\sin(n\psi) + B_n(R)\cos(n\psi)]$) and show the radial profiles of their coefficients in Figure 11. As the term $B_1(R)\cos(\psi)$ describes the rotational velocity component of the LOS velocity, we use it to build the velocity field model of the pure rotating disk. The range of the elliptical major axis is from 6″ to 80″, corresponding to the physical scale from 120 pc to 1.6 kpc. The minimum radius is set to be slightly larger than the FWHM of the PSF (5.″6) in our observation. The outermost radius is set by the requirement that at least 75% of the data are available in the elliptical annuli.

The observed velocity field of the ionized gas, the velocity field model of the pure rotating disk, the residual velocity field (subtract model from the observed map), and the *HST*606W image[10] of NGC 1042 are shown in Figure 12. The minimum error of our velocity measurements is about 6 km s^{-1}. Thus, we show the residual velocity field with velocity bin of 6 km s^{-1}. Assuming the spiral arms are trailing and considering the rotation direction of the velocity field, we determine the near side and far side of this galaxy to be southwest and northeast, respectively. The typical value of the residual velocity ranges from 0 to ∼6 km s^{-1}, which is within the error bars of the LOS velocity. For the bright star-forming regions in the spiral arms, the residual velocity can increase to ∼12 km s^{-1}. This could be the result of supersonic turbulence maintained by the energy output through supernovae and stellar winds (Scalo & Elmegreen 2004; Sellwood 2014). However, we notice that only part of the bright star-forming regions are associated with the enhancement of the residual velocity.

As shown in Figure 13, in the central 500 pc × 500 pc region, we find that the residual velocity associated with the CRIGS has a significant increase and reaches the largest value in the residual velocity field (∼20 km s^{-1}), indicating strong noncircular motions in this structure. On the near side we see redshifted velocities, and on the northeast quadrant of the far side we see blueshifted emission. This amounts to a clear signature of ionized gas inflow associated with the CRIGS. Further evidence comes from the radial profiles of different Fourier coefficients obtained from the HDM. As we introduce in Appendix A, the first-order Fourier terms ($A_1\sin(\psi)$ and $B_1\cos(\psi)$) describe the radial and rotational velocity components of the LOS velocity. The higher-order Fourier terms ($A_n\sin(n\psi)$ and $B_n\cos(n\psi)$, $n \geqq 2$) can provide information about the perturbations of the gravitational potential. As shown in Figure 11, the radial velocity component (A_1) ranges from 0 to −7 km s^{-1} in the central 8″–15″ (160–300 pc) region associated with the CRIGS. The negative sign indicates the

[10] We obtain the image from the Hubble Legacy Archive (HLA, http://hla.stsci.edu/)

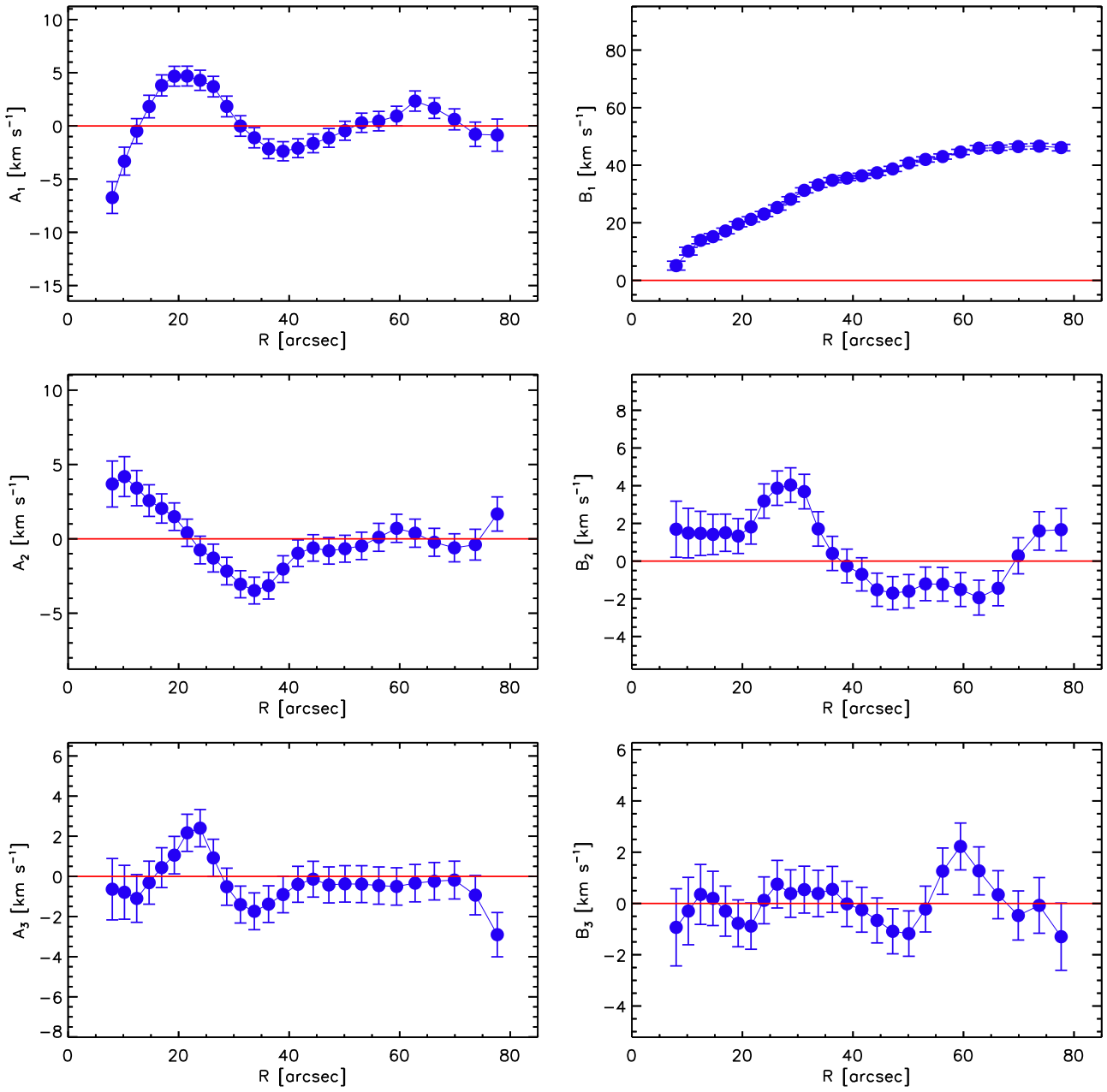

Figure 11. The radial profiles of the coefficients of different Fourier components obtained from the harmonic decomposition modeling. The range of the elliptical major axis in the harmonic decomposition modeling is from 6″ to 80″, corresponding to the physical scale from 120 pc to 1.6 kpc. The minimum radius is set to be slightly larger than the FWHM of the PSF (5.″6) in our observation. The outermost radius is set by the requirement that at least 75% of the data are available in the elliptical annuli.

inflowing feature of this component. In this region, the absolute value of this inflowing velocity component is comparable to that of the rotational velocity component (B_1), ranging from 5 to 15 km s^{-1}. Although the velocity component A_2 also has some contribution within the inner 15″ (300 pc), which may indicate the $m = 1$ potential perturbation in this region (e.g., a lopsided disk), the other higher-order velocity components (B_2, A_3, B_3) only have a limited contribution to the LOS velocity. These results suggest the ionized gas inflow is the main contributor of the noncircular motions in the CRIGS.

Interestingly, the morphology of the inflowing gas is asymmetric. As shown in Figure 13, the inflow signature is dominated by the redshifted velocities in the near side of NGC 1042. In order to quantify the significance of this asymmetry, we compare the inflow timescale (the timescale of the inflowing gas moving to the galaxy center) with the dynamical timescales in the central disk (at a radius of 300 pc (R)). Based on the measured rotation velocity ($V_{\rm rot} = B_1(R)/\sin(i) = 24$ km s^{-1}), we obtain the dynamical timescale $T_{\rm dyn} = 2\pi R/V_{\rm rot} \sim 7.7 \times 10^8$ year. In the meantime, assuming a constant inflow velocity ($V_{\rm in} = 32$ km s^{-1}, see Section 5.1 for details), we obtain the inflow timescale $T_{\rm in} = R/V_{\rm in} \sim 9.2 \times 10^7$ year. Thus, $T_{\rm dyn}$ is about eight times $T_{\rm in}$, suggesting that the gas inflows cannot last for one rotation period. Thus, the asymmetry of the inflowing gas is expected because the gas does not have time to circle the disk before it is induced to the center.

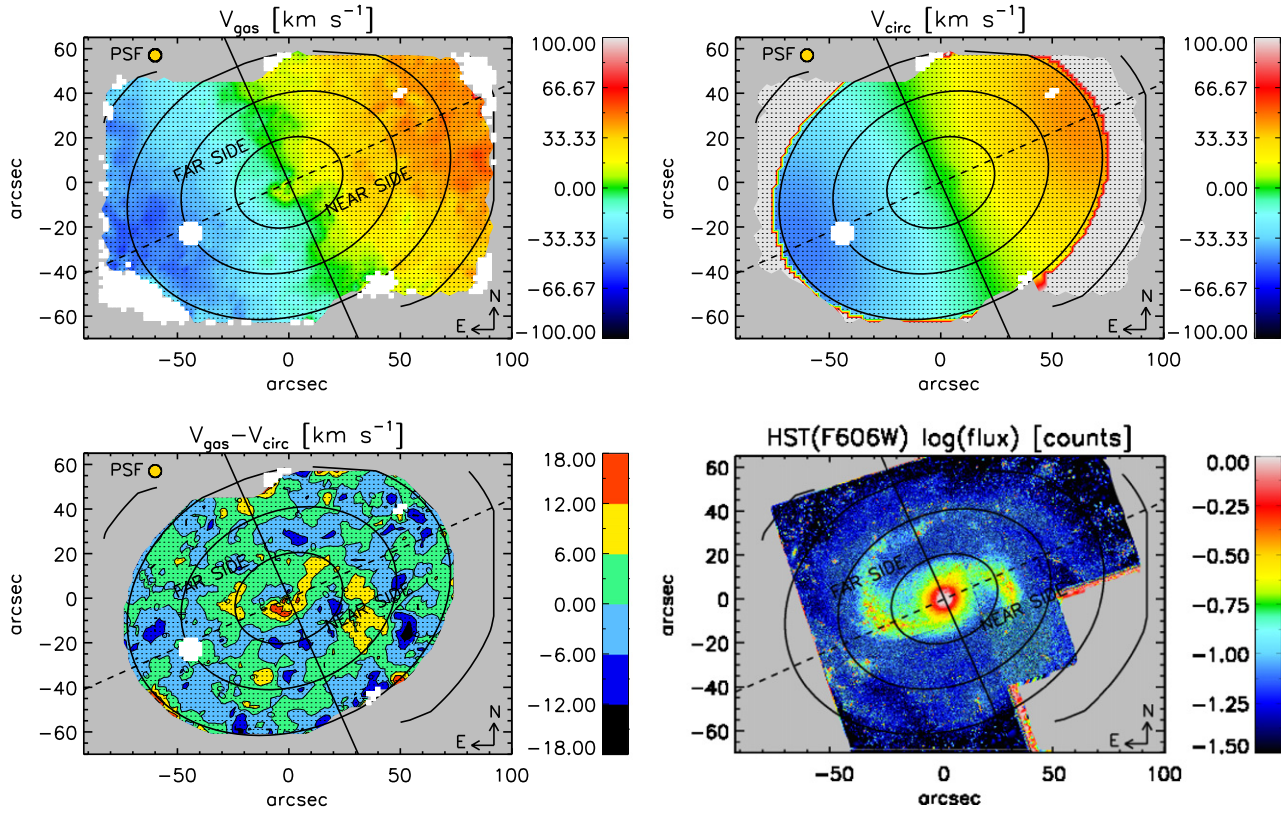

Figure 12. The observed velocity field of the ionized gas, the velocity field model of the pure rotating disk, the residual velocity field (subtract model from the observed map), and the *HST* 606W image of NGC 1042. The kinematic major axis and minor axis are shown as black dashed and solid lines, respectively. The gold circles in the top left corners present the 5.″6 FWHM PSF of the VENGA data. The black contours represent the constant radii in steps of 0.5 kpc.

In disk galaxies, the gravity torques induced by the nonaxisymmetric features (such as bars, ovals, and spiral arms) can drive gas inward to the central region of galaxies (Shlosman et al. 1989, 1990; Kormendy & Kennicutt 2004; Martini et al. 2004; Jogee 2006). The inflowing gas is usually shocked and can be traced by dust lanes (Athanassoula 1992). As we introduced in Section 1.1 and as shown in Figures 12 and 13, the inner spiral arms in NGC 1042 are very open and sharply curve toward the central region, which can produce a bar-like structure and enhance the perturbation strength of the gravitational potential (Buta et al. 2005; Buta & Zhang 2009). In Figure 13, we find that the shocked gas is located at the trailing side and at the end of the inner spiral arms. Thus, we propose that this spiral arm structure can produce a dynamical effect similar to a bar to drive the radial gas inflow. If two spiral arms are considered as the boundary of a "bar," we would expect the shocked gas inflow to appear along the trailing side of the spiral arms and at the point where the spiral arms end (Li et al. 2015), which is supported by our observation. Previous studies have found two excellent examples (NGC 4321 and M51) of secular evolution induced by spiral arms (Kormendy & Cornell 2004; Kormendy & Kennicutt 2004). In these galaxies, the regular global spiral arms directly wind down to the galaxy center and produce nuclear star formation. Our observational results of NGC 1042 provide another example of spiral arm–induced gas inflows in disk galaxies.

5. DISCUSSION

In Section 4 we demonstrate that the CRIGS is shock excited, and the shock is produced by the inflow of the ionized gas driven by the inner spiral arms in NGC 1042. Here we estimate the mass-inflow rate of the ionized gas and further discuss its implications for the AGN feeding and star formation in the nuclear star cluster.

5.1. Mass-inflow Rate of the Ionized Gas

As shown in Section 4.2, the observed LOS velocity in the CRIGS is mainly dominated by the inflowing velocity component (A_1 term). In order to quantify this and separate the radial flow (which points toward the center and may feed the nuclear activities) and the azimuthal streaming flow (which may just circle around the CRIGS and not contribute to the feeding of the nuclear activities), we decompose the residual velocity field shown in Figure 12 into two Fourier terms, as $V_{\rm res}(R, \psi) = C_1(R)\sin(\psi) + S_1(R)\cos(\psi)$. The components $C_1(R)\sin(\psi)$ and $S_1(R)\cos(\psi)$ correspond to the radial flow component and the azimuthal streaming component, respectively. We again use the Kinemetry software to execute the decomposition, and we show the results in Figure 14. The top panel shows the C_1 and S_1 as a function of radius. It shows that the radial inflow dominates the residual velocity and the azimuthal streaming flow is negligible. In the bottom panel of Figure 14, we also show the azimuthal distribution of the components $C_1\sin(\psi)$, $S_1\cos(\psi)$, and their sum at the annulus with a radius of 150 pc (the median radius of the CRIGS). In the whole annulus, the azimuthal streaming flow is negligible. Thus, we use the whole residual velocity ($\sim$20 $\pm$ 6 km s^{-1}) associated with the CRIGS to approximate the inflow velocity along the LOS. By adopting the inclination angle of 38.°7, we obtain the deprojected inflow velocity as $V_{\rm in} \sim 32 \pm 10$ km s^{-1}.

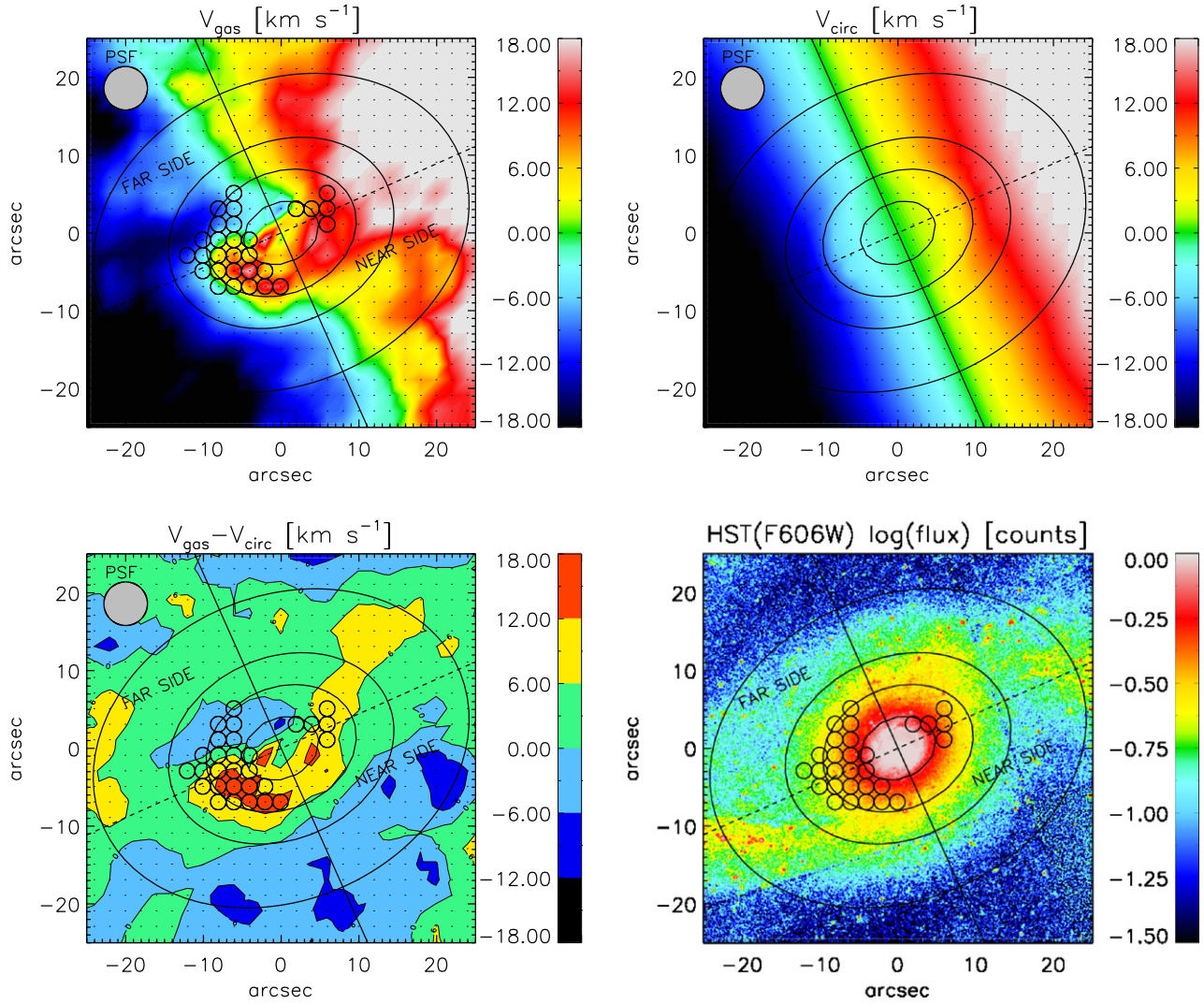

Figure 13. The observed velocity field of the ionized gas, the velocity field model of the pure rotating disk, the residual velocity field (subtract model from the observed map), and the *HST* 606W image of the central 500 pc × 500 pc region in NGC 1042. The kinematic major axis and minor axis are shown as black dashed and solid lines, respectively. Small black circles mark the CRIGS. The gray circles in the top left corners present the 5.″6 FWHM PSF of the VENGA data. The black contours represent the constant radii of 0.1, 0.2, 0.3, and 0.5 kpc.

Having estimated the inflow velocity, we now estimate the mass-inflow rate of the ionized gas. Since the CRIGS has a ring-like morphology, we assume that the inflowing gas is ring-like at radius r and with height h, and we calculate the integral of the flux of matter through a cylindrical area of radius r and height h. Thus the mass-inflow rate can be described as below:

$$\dot{M}_{\rm in} = 2\,\pi\,r\,h\,n_e\,m_p f\,V_{\rm in} \quad (1)$$

where n_e is the electron density, m_p is the mass of the proton, f is the filling factor of the ionized gas, and $V_{\rm in}$ is the deprojected inflow velocity.

We can estimate r and h based on the position and size of the inflow region. We use the outer boundary of the CRIGS as the border of the inflow region, so r is about 300 pc. The inflow region extends from 100 to 300 pc from the galaxy center, so the radial span of this region is $\Delta r \sim 200$ pc. Assuming the value of h has an order of magnitude similar to that of the radial span of the inflow region, and considering the projection effect, h should be $\Delta r \times \sin(i)$, which gives ∼70 pc. Even though this is an assumption, h cannot be larger than this value, otherwise the inflow region would appear wider. Therefore, $\Delta r \times \sin(\mathrm{i})$ can be considered as an upper limit of h. Adopting an average $n_e \sim 10$ cm^{-3} (see Figure 9) and $f = 0.001$ (Schnorr Müller et al. 2011), we obtain the mass-inflow rate as $\dot{M}_{\rm in} \sim 1.1 \pm 0.3 \times 10^{-3}\,M_\odot$ yr^{-1}. The uncertainty on the distance of NGC 1042 (described in Section 1.1) can affect the value of r, h, and the estimation of the mass-inflow rate; thus, we also calculate the mass-inflow rate corresponding to the distance of NGC 1042 at 8 Mpc, which is $\dot{M}_{\rm in}\sim 2.1 \pm 0.3 \times 10^{-3}\,M_\odot$ yr^{-1}.

5.2. Implication for Feeding the Nuclear Activities

The mass-accretion rate ($\dot{M}$) at the last stable orbit of the black hole can be calculated as

$$\dot{M} = \frac{L_{\rm bol}}{c^2\eta} \quad (2)$$

where c is the velocity of light, $L_{\rm bol}$ is the bolometric luminosity of the AGN, and η is the radiation efficiency,

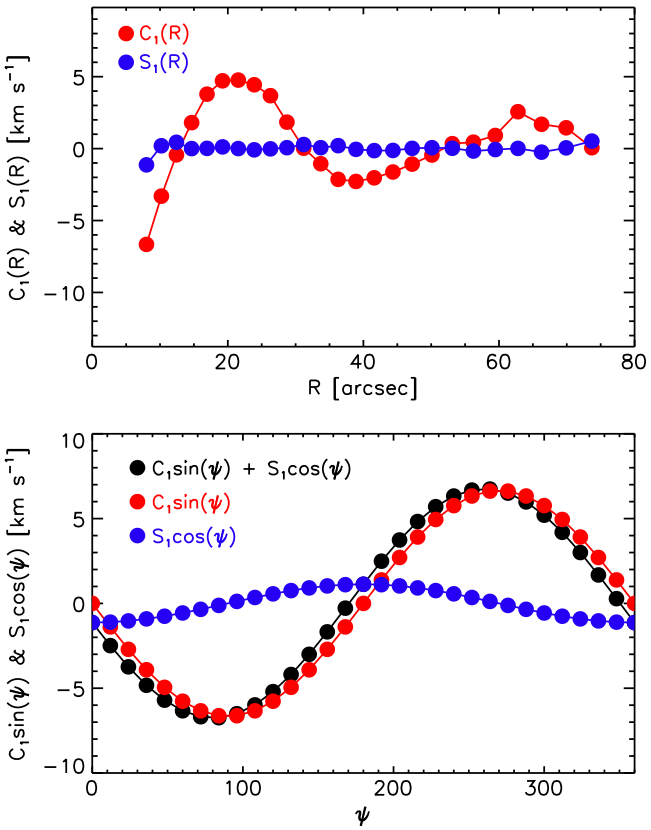

Figure 14. Top panel: radial profiles of the coefficients of $C_1(R)$ and $S_1(R)$ in the residual velocity. The range of the elliptical major axis in the decomposition process is from 6″ to 75″, corresponding to the physical scale from 120 pc to 1.5 kpc. The minimum radius is set to be slightly larger than the FWHM of the PSF (5.″6) in our observation. The outermost radius is set by the requirement that at least 75% of the data are available in the elliptical annuli. Bottom panel: azimuthal distributions of the Fourier components $C_1\sin(\psi)$ and $S_1\cos(\psi)$ at the annulus with a radius of 150 pc (the median radius of the CRIGS). The error bars are smaller than the data symbols shown in the figure and thus are not visible.

which describes the efficiency of the accreted mass energy converted into radiation. Here, η depends on the nature of different accretion disks and flows. For LINERs, it has been suggested that the accretion disk is geometrically thick and optically thin (Nemmen et al. 2006; Yuan et al. 2007). This kind of accretion flow is known as RIAF (radiatively inefficient accretion flow; Narayan 2005) and has a typical value of $\eta \sim 0.01$. Using the bolometric luminosity of 8.0×10^{39} erg s^{-1} for NGC 1042 (Shields et al. 2008), we obtain the mass-accretion rate $\dot{M} \sim 1.4 \times 10^{-5}\ M_\odot$ yr^{-1}.

The mass-inflow rate described in Section 5.1 is about 100 times the mass-accretion rate. This result suggests that the inflowing gas is sufficient to feed the AGN activity in NGC 1042, and only a small portion (a few percent) may be transferred into the center to feed the black hole. This is in agreement with many previous studies. As discussed in Ho (2008, 2009), most LLAGNs in the nearby universe reside in a low or quiescent state and undergo radiatively inefficient accretion, even though fuel is plentiful in the central region of these galaxies. They show that the local processes (e.g., mass loss from evolved stars and Bondi accretion of hot gas) can provide sufficient fuel for nuclear activity. Based on the lack of correlation of black holes with disks and pseudobulges, Kormendy et al. (2011) and Kormendy & Ho (2013) also proposed that the local stochastic processes can feed the growth of black holes in disk-dominated galaxies at redshift ∼0. In addition, Genzel et al. (2010) summarized the effective mass-accretion rate from a few hundred parsecs to several Schwarzschild radii in the Milky Way and proposed that the angular momentum transport of the gas surrounding the Galactic center black hole could be inefficient. High-spatial-resolution observations (e.g., Thirty Meter Telescope, Atacama Large Millimeter/submillimeter Array) will be important for the study of AGN feeding within 100 pc of galaxies, which can help us to understand the relationship between the accretion process of black holes and their surrounding materials.

In addition to the AGN activity, the nuclear star cluster in NGC 1042 has a young stellar population component with an age of ∼10 Myr and a mass of $\sim 7.94 \times 10^3\ M_\odot$. This implies an average star-formation rate of $\sim 7.94 \times 10^{-4}\ M_\odot$ yr^{-1} in this component. The mass-inflow rate we obtained above has an order of magnitude similar to that of this star-formation rate, which means the inflowing gas is sufficient to feed star formation in the nuclear star cluster and make it grow.

6. SUMMARY

Using the IFS data from the VENGA survey, we have explored the feeding process of the LLAGN in the late-type bulgeless galaxy NGC 1042. The large spatial coverage of the Mitchell spectrograph observation (3.5 kpc × 2.5 kpc) enables us to map the emission of the ionized gas from several kiloparsecs down to several hundred parsecs in this galaxy. By studying the excitation and kinematic properties of the ionized gas using various emission-line properties, we directly identify the radial gas inflows in the central 500 pc × 500 pc of the galaxy.

From the flux and flux ratio maps of emission lines (including [O II]$\lambda\lambda$ 3726, 3729, [O III]λ5007, Hα, Hβ, [N II] λ6548, 6583, and [S II]λ6717, 6731), we find a circumnuclear ring-like structure of ionized gas (which we call CRIGS) in the central 100–300 pc region. Using the spatially resolved BPT diagnostics, we find that this structure presents LINER-like emission. By comparing with the predictions of shock ionization models, we conclude that shocks are the dominant ionization source in this structure. This result is also supported by the disturbed kinematics of the ionized gas (the distorted velocity field and enhanced velocity dispersion) in this structure.

The harmonic decomposition modeling (HDM) is used to analyze the velocity field of the ionized gas and quantify the possible noncircular motions driven by the gas flows. We do not find significant noncircular motions of the ionized gas at large radii of the disk. Strong noncircular motions of the ionized gas only exist within the central 500 pc × 500 pc, especially at the CRIGS. On the near side we see redshifted velocities, and on the northeast quadrant of the far side we see blueshifted emission, indicating that the ionized gas in the CRIGS is inflowing. Combining with the *HST* image of NGC 1042, we find that the CRIGS takes place at the end of the inner spiral arms. Since the inner spiral arms in NGC 1042 sharply curve toward the central region, producing a bar-like structure, we propose that the inner spiral arms of NGC 1042 can produce a dynamical effect similar to a bar to drive the shocked ionized gas inflow.

We calculate the deprojected inflow velocity at $\sim 32 \pm 10$ km s^{-1} and further estimate the mass-inflow rate at $\sim 1.1 \pm 0.3 \times 10^{-3}\ M_{\odot}$ yr^{-1}. The mass-inflow rate is about one hundred times the BH's mass-accretion rate ($\sim 1.4 \times 10^{-5}\ M_{\odot}$ yr^{-1}) and at an order of magnitude similar to that of the star-formation rate in the nuclear star cluster ($7.94 \times 10^{-4}\ M_{\odot}$ yr^{-1}). It is large enough to feed both the nuclear activity and the star formation in the nuclear star cluster. The BH's mass-accretion rate is significantly less than the mass-inflow rate, suggesting that only a small portion of these materials may be transferred into the center to feed the black hole. Although the exact feeding processes of the nuclear activity need to be further explored via high-spatial-resolution observations within the central 100 pc region, our study highlights that secular evolution can be important in late-type unbarred galaxies like NGC 1042.

We thank the anonymous referee for his or her careful and helpful comments, which improved the quality of the paper immensely. We also thank Ramya Sethuram for her help in refining the paper. R.L. and L.H. acknowledge support from the National Natural Science Foundation of China under grants No. 11473305, by the Strategic Priority Research Program "The Emergence of Cosmological Structures" of the Chinese Academy of Sciences, Grant No. XDB09030200. G.B. is supported by CONICYT/FONDECYT, Programa de Iniciacion, Folio 11150220. S.J. acknowledges support from NSF grant NSF AST-1413652 and the National Aeronautics and Space Administration (NASA) JPL SURP Program. The construction of the Mitchell Spectrograph (formerly VIRUS-P) was possible thanks to the generous support of the Cynthia & George Mitchell Foundation. We thank Phillip McQueen and Gary Hill for designing and constructing VIRUS-P, and for their advice on the use of the instrument. We also acknowledge David Doss and the staff at McDonald Observatory for their invaluable help during the observations. We acknowledge the usage of the HyperLeda database (http://leda.univ-lyon1.fr). This research has made use of the NASA/IPAC Extragalactic Database (NED), which is operated by the Jet Propulsion Laboratory, California Institute of Technology, under contract with the National Aeronautics and Space Administration.

APPENDIX A
HARMONIC DECOMPOSITION MODELING

Harmonic decomposition modeling (HDM) can decompose the LOS velocity field of a galaxy into a series of Fourier components that are considered as kinematic components with different azimuthal symmetry. By matching the kinematic symmetry of the observed velocity field, these components can be used to construct a model velocity field. This method has been used to study the stellar and gas kinematics in late-type galaxies (Binney 1978; Begeman 1987; Teuben 1991; Franx et al. 1994; Schoenmakers et al. 1997; Wong et al. 2004), early-type galaxies (Krajnović et al. 2006; Emsellem et al. 2007; Krajnović et al. 2008, 2011, 2013), and high-z merging systems (Shapiro et al. 2008; Gonçalves et al. 2010; Alaghband-Zadeh et al. 2012; Bellocchi et al. 2012; Swinbank et al. 2012).

The Fourier components in the HDM are obtained in a set of elliptical annuli along the semimajor axis of a galaxy. The shapes of these elliptical annuli are described by their geometry parameters, including the positions of the centers, position angles (P.A.), and inclinations. For each elliptical annulus, the LOS velocity is fitted as

$$V_{\rm LOS}(R,\ \psi) = A_0(R) + \sum_{n=1}^{k}[A_n(R)\sin(n\psi) + B_n(R)\cos(n\psi)] \quad (3)$$

where R is the semimajor axis of the elliptical annuli, ψ is the eccentric anomaly angle, and A_0, A_n, and B_n are the corresponding coefficients of different Fourier components. The zero-order term (A_0) is the systemic velocity of the galaxy. The first-order terms ($A_1\sin(\psi)$ and $B_1\cos(\psi)$) describe the radial and rotational velocity components. The higher-order terms ($A_n\sin(n\psi)$ and $B_n\cos(n\psi)$, $n \geqq 2$) can provide information about the perturbations of gravitational potential (Schoenmakers et al. 1997; Wong et al. 2004).

In disk galaxies, we assume the gas is located on the galaxy plane and ignore the motions in the vertical direction. The LOS velocity along each elliptical annulus of a pure rotating disk can be described as $V_{\rm LOS}(R,\ \psi) = A_0 + B_1(R)\cos(\psi)$. In this case, the geometry parameters of elliptical annuli and the system velocity do not change with R. The other Fourier components in Equation (1) describe the departures from circular rotation, which can be used to quantify different gas flows in disk galaxies.

APPENDIX B
DETERMINING DISK PARAMETERS

In general, the kinematic center is consistent with the photometric center in galaxies (Haan et al. 2008; Trachternach et al. 2008; Neumayer et al. 2011; Andersen & Bershady 2013). Considering the effective PSF FWHM of 5.″6 in our data cube, we assume the kinematic center and photometric center are in agreement and use the photometric center from SDSS DR8 (Aihara et al. 2011) as the center coordinates ($02^{\rm h}40^{\rm m}23^{\rm s}.967$, $-08°26'00''.76$) of NGC 1042. This parameter will be fixed in the subsequent analysis.

In order to determine the system velocity, position angle (P.A.), and inclination of NGC 1042, we first use Kinemetry (Krajnović et al. 2006) to quantify the observed velocity field of the ionized gas and present the radial profiles of these parameters. As shown in Figure 15, all parameters have significant variances within the inner 40″, which could be caused by the kinematic twist that is due to gas flow in this region and the existence of the inner spiral arms. While in the outer $40'' < R < 80''$, these parameters show a relatively flat profile and the kinematics also presents the signature of regular circular motion. Therefore, we determine the system velocity, P.A., and inclination of NGC 1042 to be the radial average of these parameters within $40'' < R < 80''$. The obtained system velocity, kinematic P.A., and flattening[11] are 1366.3 ± 3 km s^{-1}, $114.°0 \pm 1°$, and 0.78 ± 0.5 (corresponding to a kinematic inclination of $38.°7 \pm 0.°5$), respectively.

We also use IDL routine FIT_KINEMATIC_PA[12] to measure the kinematic P.A. and system velocity, which can provide a double check on the values obtained above. In this code, the symmetrization method (see Appendix C of Krajnović et al. 2006) is performed, which minimizes the differences between the observed velocity field and a

[11] The flattening q = cos(i).
[12] http://www-astro. physics.ox.ac.uk/~mxc/software/

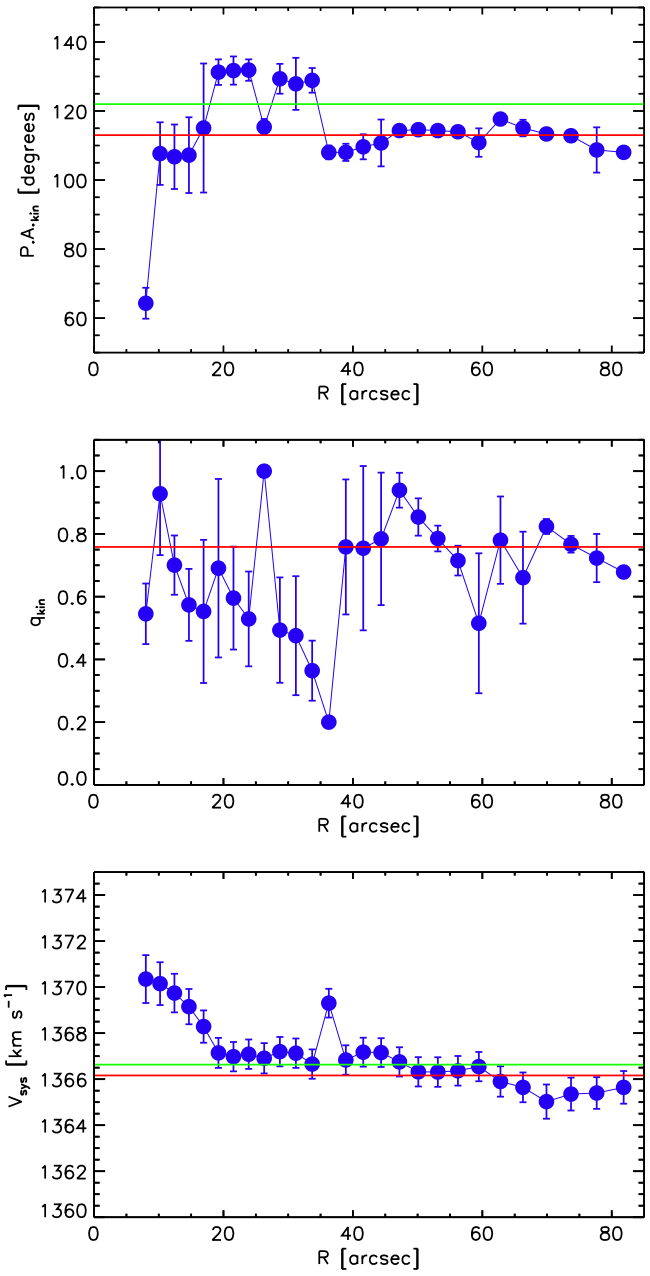

Figure 15. The radial profile of the kinematic P.A., the flattening, and the system velocity of NGC 1042 obtained from Kinemetry. The range of the elliptical major axis in Kinemetry is from 6″ to 80″, corresponding to the physical scale from 120 pc to 1.6 kpc. The minimum radius is set to be slightly larger than the FWHM of the PSF (5.″6) in our observation. The outermost radius is set by the requirement that at least 75% of the data are available in the elliptical annuli. The red solid lines show the average values of these parameters within $40'' < R < 80''$. The green solid lines present the kinematic P.A. and the system velocity obtained from FIT_KINEMATIC_PA.

biantisymmetric velocity field to obtain the kinematic P.A. and system velocity. The obtained kinematic P.A. and system velocity are $122° \pm 0.°5$ and 1367 ± 4 km s^{-1}, respectively. While the system velocity is consistent with the value obtained from the radial average, the kinematic P.A. has a difference of $\sim 8°$, which could be due to the kinematic twist in the inner region of NGC 1042. We prefer to adopt the kinematic P.A. obtained from the radial average at $114.°0 \pm 1°$.

The disk parameters of NGC 1042 can also be measured from other observations. We compare these measurements with our kinematic results. Integrated H I and optical observations have provided several measurements of the system velocity of NGC 1042: 1371 ± 2 km s^{-1} (Koribalski et al. 2004), 1371 ± 1 km s^{-1} (Springob et al. 2005), and 1372 ± 3 km s^{-1} (compilation of Hyperleda[13]). These measurements are in agreement with the system velocity we derived here within the error range.

The photometric P.A. of NGC 1042 measured from SDSS r-band and 2MASS K-band images are 84° (Adelman-McCarthy et al. 2008) and 145° (Jarrett et al. 2003), which are in significant disagreement with the kinematic P.A. obtained above. The discrepancy between photometric and kinematic P.A. in many other galaxies has been observed in the GHASP (Epinat et al. 2008), SAURON (Krajnović et al. 2008), Atlas 3D (Krajnović et al. 2011), and CALIFA surveys (García-Lorenzo et al. 2015). The photometric P.A. has large systematic uncertainties associated with its covariance with the inclination, and with possible photometric deviations from axisymetry in disks, which can also be color dependent. Thus we prefer to adopt the kinematically derived position angle.

In terms of inclination, we use the photometric axis ratios to derive the photometric inclination of NGC 1042. By adopting the method of Tully (1988), we obtain $i = 40°$ for RC3 B-band measurement (de Vaucouleurs et al. 1991) and $i = 37°$ for 2MASS K-band photometry (Jarrett et al. 2003). All of these inclination measurements are consistent with the obtained kinematic inclination.

The final disk parameters used in the kinematic analysis are as follows: center position at $02^h40^m23.^s967$, $-08°26'00.''76$; system velocity at 1366.3 ± 3 km s^{-1}; P.A. at $114.°0 \pm 1°$; and inclination at $38.°7 \pm 0.°5$.

REFERENCES

Adams, J. J., Blanc, G. A., Hill, G. J., et al. 2011, ApJS, 192, 5
Adelman-McCarthy, J. K., Agüeros, M. A., Allam, S. S., et al. 2008, ApJS, 175, 297
Aihara, H., Allende Prieto, C., An, D., et al. 2011, ApJS, 193, 29
Alaghband-Zadeh, S., Chapman, S. C., Swinbank, A. M., et al. 2012, MNRAS, 424, 2232
Andersen, D. R., & Bershady, M. A. 2013, ApJ, 768, 41
Arribas, S., Colina, L., Bellocchi, E., Maiolino, R., & Villar-Martín, M. 2014, A&A, 568, A14
Athanassoula, E. 1992, MNRAS, 259, 345
Athanassoula, E. 2008, MNRAS, 390, L69
Baldwin, J. A., Phillips, M. M., & Terlevich, R. 1981, PASP, 93, 5
Barnes, J. E., & Hernquist, L. E. 1991, ApJL, 370, L65
Begeman, K. G. 1987, PhD thesis, Kapteyn Institute
Bellocchi, E., Arribas, S., & Colina, L. 2012, A&A, 542, A54
Binette, L. 1985, A&A, 143, 334
Binette, L., Magris, C. G., Stasińska, G., & Bruzual, A. G. 1994, A&A, 292, 13
Binney, J. 1978, MNRAS, 183, 779
Blanc, G. A., Heiderman, A., Gebhardt, K., Evans, N. J., II, & Adams, J. 2009, ApJ, 704, 842
Blanc, G. A., Kewley, L., Vogt, F. P. A., & Dopita, M. A. 2015, ApJ, 798, 99
Blanc, G. A., Weinzirl, T., Song, M., et al. 2013, AJ, 145, 138
Bland-Hawthorn, J., Sokolowski, J., & Cecil, G. 1991, ApJ, 375, 78
Böker, T., Laine, S., van der Marel, R. P., et al. 2002, AJ, 123, 1389
Böker, T., Sarzi, M., McLaughlin, D. E., et al. 2004, AJ, 127, 105
Buta, R., Vasylyev, S., Salo, H., & Laurikainen, E. 2005, AJ, 130, 506
Buta, R. J., & Zhang, X. 2009, ApJS, 182, 559
Cappellari, M., & Emsellem, E. 2004, PASP, 116, 138
Cheung, E., Trump, J. R., Athanassoula, E., et al. 2015, MNRAS, 447, 506
Cid Fernandes, R., Stasińska, G., Mateus, A., & Vale Asari, N. 2011, MNRAS, 413, 1687
Cid Fernandes, R., Stasińska, G., Schlickmann, M. S., et al. 2010, MNRAS, 403, 1036

[13] http://leda.univ-lyon1.fr/

Cisternas, M., Gadotti, D. A., Knapen, J. H., et al. 2013, ApJ, 776, 50
Cisternas, M., Jahnke, K., Inskip, K. J., et al. 2011, ApJ, 726, 57
Cisternas, M., Sheth, K., Salvato, M., et al. 2015, ApJ, 802, 137
Combes, F., García-Burillo, S., Casasola, V., et al. 2014, A&A, 565, A97
Comerón, S., Knapen, J. H., Beckman, J. E., et al. 2010, MNRAS, 402, 2462
Comerón, S., Salo, H., Laurikainen, E., et al. 2014, A&A, 562, A121
Davies, R. I., Maciejewski, W., Hicks, E. K. S., et al. 2009, ApJ, 702, 114
Davies, R. I., Maciejewski, W., Hicks, E. K. S., et al. 2014, ApJ, 792, 101
de Vaucouleurs, G., de Vaucouleurs, A., Corwin, H. G., Jr., et al. 1991, Third Reference Catalogue of Bright Galaxies, (Vols. I, II, III; New York: Springer)
Di Matteo, T., Springel, V., & Hernquist, L. 2005, Natur, 433, 604
Dong, X.-B., Ho, L. C., Yuan, W., et al. 2012, ApJ, 755, 167
Dopita, M. A., Payne, J. L., Filipović, M. D., & Pannuti, T. G. 2012, MNRAS, 427, 956
Dopita, M. A., & Sutherland, R. S. 1995, ApJ, 455, 468
Dopita, M. A., & Sutherland, R. S. 1996, ApJS, 102, 161
Dopita, M. A., & Sutherland, R. S. 2003, Astrophysics of the diffuse universe (New York: Springer)
Dumas, G., Mundell, C. G., Emsellem, E., & Nagar, N. M. 2007, MNRAS, 379, 1249
Elmegreen, D. M., & Elmegreen, B. G. 1987, ApJ, 314, 3
Emsellem, E., Cappellari, M., Krajnović, D., et al. 2007, MNRAS, 379, 401
Epinat, B., Amram, P., Marcelin, M., et al. 2008, MNRAS, 388, 500
Falcón-Barroso, J., Sánchez-Blázquez, P., Vazdekis, A., et al. 2011, A&A, 532, A95
Farage, C. L., McGregor, P. J., Dopita, M. A., & Bicknell, G. V. 2010, ApJ, 724, 267
Fathi, K., Lundgren, A. A., Kohno, K., et al. 2013, ApJL, 770, L27
Fathi, K., Storchi-Bergmann, T., Riffel, R. A., et al. 2006, ApJL, 641, L25
Ferland, G. J., & Netzer, H. 1983, ApJ, 264, 105
Ferrarese, L., Ford, H. C., Huchra, J., et al. 2000, ApJS, 128, 431
Franx, M., van Gorkom, J. H., & de Zeeuw, T. 1994, ApJ, 436, 642
Freedman, W. L., Madore, B. F., Gibson, B. K., et al. 2001, ApJ, 553, 47
Galloway, M. A., Willett, K. W., Fortson, L. F., et al. 2015, MNRAS, 448, 3442
Ganda, K., Falcón-Barroso, J., Peletier, R. F., et al. 2006, MNRAS, 367, 46
García-Burillo, S., & Combes, F. 2012, JPhCS, 372, 012050
García-Lorenzo, B., Márquez, I., Barrera-Ballesteros, J. K., et al. 2015, A&A, 573, A59
Gebhardt, K., Bender, R., Bower, G., et al. 2000, ApJL, 539, L13
Genzel, R., Eisenhauer, F., & Gillessen, S. 2010, RvMP, 82, 3121
Gonçalves, T. S., Basu-Zych, A., Overzier, R., et al. 2010, ApJ, 724, 1373
Greene, J. E. 2012, NatCo, 3, 1304
Greene, J. E., & Ho, L. C. 2004, ApJ, 610, 722
Greene, J. E., & Ho, L. C. 2007, ApJ, 670, 92
Greene, J. E., Peng, C. Y., Kim, M., et al. 2010, ApJ, 721, 26
Groves, B. A., Dopita, M. A., & Sutherland, R. S. 2004, ApJS, 153, 75
Haan, S., Schinnerer, E., Mundell, C. G., García-Burillo, S., & Combes, F. 2008, AJ, 135, 232
Haffner, L. M., Dettmar, R.-J., Beckman, J. E., et al. 2009, RvMP, 81, 969
Haffner, L. M., Reynolds, R. J., & Tufte, S. L. 1999, ApJ, 523, 223
Halpern, J. P., & Steiner, J. E. 1983, ApJL, 269, L37
Hicks, E. K. S., Davies, R. I., Maciejewski, W., et al. 2013, ApJ, 768, 107
Hill, G. J., Gebhardt, K., Komatsu, E., et al. 2008, in ASP Conf. Ser. 399, Panoramic Views of Galaxy Formation and Evolution, ed. T. Kodama, T. Yamada, & K. Aoki (San Francisco, CA: ASP), 115
Ho, I.-T., Kewley, L. J., Dopita, M. A., et al. 2014, MNRAS, 444, 3894
Ho, L. C. 2008, ARA&A, 46, 475
Ho, L. C. 2009, ApJ, 699, 626
Ho, L. C., Filippenko, A. V., & Sargent, W. L. W. 1993, ApJ, 417, 63
Ho, L. C., Filippenko, A. V., & Sargent, W. L. W. 1997, ApJ, 487, 591
Hoopes, C. G., & Walterbos, R. A. M. 2003, ApJ, 586, 902
Hopkins, P. F., Hernquist, L., Cox, T. J., et al. 2006, ApJS, 163, 1
Hopkins, P. F., Hernquist, L., Cox, T. J., & Kereš, D. 2008, ApJS, 175, 356
Hu, J. 2008, MNRAS, 386, 2242
Hunt, L. K., & Malkan, M. A. 1999, ApJ, 516, 660
Jarrett, T. H., Chester, T., Cutri, R., et al. 2000, AJ, 119, 2498
Jarrett, T. H., Chester, T., Cutri, R., Schneider, S. E., & Huchra, J. P. 2003, AJ, 125, 525
Jogee, S. 2006, in Physics of Active Galactic Nuclei at all Scales, Vol. 693, ed. D. Alloin (Springer: Berlin), 143
Jogee, S., Scoville, N., & Kenney, J. D. P. 2005, ApJ, 630, 837
Jogee, S., Shlosman, I., Laine, S., et al. 2002, ApJ, 575, 156
Kaplan, K. F., et al. 2016, MNRAS submitted
Karouzos, M., Jarvis, M. J., & Bonfield, D. 2014, MNRAS, 439, 861
Kartaltepe, J. S., Sanders, D. B., Le Floc'h, E., et al. 2010, ApJ, 721, 98
Kauffmann, G., & Haehnelt, M. 2000, MNRAS, 311, 576
Kauffmann, G., Heckman, T. M., Tremonti, C., et al. 2003, MNRAS, 346, 1055
Kehrig, C., Monreal-Ibero, A., Papaderos, P., et al. 2012, A&A, 540, A11
Kewley, L. J., Dopita, M. A., Sutherland, R. S., Heisler, C. A., & Trevena, J. 2001, ApJ, 556, 121
Kewley, L. J., Groves, B., Kauffmann, G., & Heckman, T. 2006, MNRAS, 372, 961
Kocevski, D. D., Faber, S. M., Mozena, M., et al. 2012, ApJ, 744, 148
Koribalski, B. S., Staveley-Smith, L., Kilborn, V. A., et al. 2004, AJ, 128, 16
Kormendy, J., Bender, R., & Cornell, M. E. 2011, Natur, 469, 374
Kormendy, J., & Cornell, M. E. 2004, in Penetrating Bars Through Masks of Cosmic Dust, Vol. 319, ed. D. L. Block et al. (Dordrecht: Kluwer), 261
Kormendy, J., & Ho, L. C. 2013, ARA&A, 51, 511
Kormendy, J., & Kennicutt, R. C., Jr. 2004, ARA&A, 42, 603
Koss, M., Mushotzky, R., Veilleux, S., et al. 2011, ApJ, 739, 57
Krajnović, D., Alatalo, K., Blitz, L., et al. 2013, MNRAS, 432, 1768
Krajnović, D., Bacon, R., Cappellari, M., et al. 2008, MNRAS, 390, 93
Krajnović, D., Cappellari, M., de Zeeuw, P. T., & Copin, Y. 2006, MNRAS, 366, 787
Krajnović, D., Emsellem, E., Cappellari, M., et al. 2011, MNRAS, 414, 2923
Laine, S., Shlosman, I., Knapen, J. H., & Peletier, R. F. 2002, ApJ, 567, 97
Laurikainen, E., & Salo, H. 2002, MNRAS, 337, 1118
Laurikainen, E., Salo, H., & Buta, R. 2004a, ApJ, 607, 103
Laurikainen, E., Salo, H., Buta, R., & Vasylyev, S. 2004b, MNRAS, 355, 1251
Lee, G.-H., Park, C., Lee, M. G., & Choi, Y.-Y. 2012, ApJ, 745, 125
Li, Z., Shen, J., & Kim, W.-T. 2015, ApJ, 806, 150
Li, Z.-Y., Ho, L. C., Barth, A. J., & Peng, C. Y. 2011, ApJS, 197, 22
Madsen, G. J., Reynolds, R. J., & Haffner, L. M. 2006, ApJ, 652, 401
Malkan, M. A., Gorjian, V., & Tam, R. 1998, ApJS, 117, 25
Marinova, I., & Jogee, S. 2007, ApJ, 659, 1176
Martini, P. 2004, in IAU Symp. 222, The Interplay Among Black Holes, Stars and ISM in Galactic Nuclei, ed. T. Storchi-Bergmann, L. C. Ho, & H. R. Schmitt (Cambridge: Cambridge Univ. Press), 235
Martini, P., Regan, M. W., Mulchaey, J. S., & Pogge, R. W. 2003, ApJ, 589, 774
Mathis, J. S. 2000, ApJ, 544, 347
McConnell, N. J., & Ma, C.-P. 2013, ApJ, 764, 184
McDonald, M., Veilleux, S., & Rupke, D. S. N. 2012, ApJ, 746, 153
Mihos, J. C., & Hernquist, L. 1996, ApJ, 464, 641
Monreal-Ibero, A., Arribas, S., & Colina, L. 2006, ApJ, 637, 138
Mulchaey, J. S., & Regan, M. W. 1997, ApJL, 482, L135
Müller Sánchez, F., Davies, R. I., Genzel, R., et al. 2009, ApJ, 691, 749
Narayan, R. 2005, Ap&SS, 300, 177
Negroponte, J., & White, S. D. M. 1983, MNRAS, 205, 1009
Nemmen, R. S., Storchi-Bergmann, T., Yuan, F., et al. 2006, ApJ, 643, 652
Neumayer, N., Walcher, C. J., Andersen, D., et al. 2011, MNRAS, 413, 1875
Oh, S., Oh, K., & Yi, S. K. 2012, ApJS, 198, 4
Osterbrock, D. E., & Ferland, G. J. 2006, Astrophysics of gaseous nebulae and active galactic nuclei (2nd ed,; Sausalito, CA: University Science Books)
Pei, Y. C. 1992, ApJ, 395, 130
Pequignot, D. 1984, A&A, 131, 159
Quinn, P. J., Hernquist, L., & Fullagar, D. P. 1993, ApJ, 403, 74
Reines, A. E., Greene, J. E., & Geha, M. 2013, ApJ, 775, 116
Reynolds, R. J., Haffner, L. M., & Tufte, S. L. 1999, ApJL, 525, L21
Rich, J. A., Dopita, M. A., Kewley, L. J., & Rupke, D. S. N. 2010, ApJ, 721, 505
Rich, J. A., Kewley, L. J., & Dopita, M. A. 2011, ApJ, 734, 87
Riffel, R. A., & Storchi-Bergmann, T. 2011, MNRAS, 411, 469
Riffel, R. A., Storchi-Bergmann, T., & Winge, C. 2013, MNRAS, 430, 2249
Riffel, R. A., Storchi-Bergmann, T., Winge, C., et al. 2008, MNRAS, 385, 1129
Rosario, D. J., Santini, P., Lutz, D., et al. 2012, A&A, 545, A45
Sánchez-Blázquez, P., Peletier, R. F., Jiménez-Vicente, J., et al. 2006, MNRAS, 371, 703
Sanders, D. B., Soifer, B. T., Elias, J. H., et al. 1988, ApJ, 325, 74
Sani, E., Marconi, A., Hunt, L. K., & Risaliti, G. 2011, MNRAS, 413, 1479
Sarzi, M., Falcón-Barroso, J., Davies, R. L., et al. 2006, MNRAS, 366, 1151
Sarzi, M., Shields, J. C., Schawinski, K., et al. 2010, MNRAS, 402, 2187
Scalo, J., & Elmegreen, B. G. 2004, ARA&A, 42, 275
Schawinski, K., Simmons, B. D., Urry, C. M., Treister, E., & Glikman, E. 2012, MNRAS, 425, L61
Schawinski, K., Treister, E., Urry, C. M., et al. 2011, ApJL, 727, L31
Schawinski, K., Urry, C. M., Virani, S., et al. 2010, ApJ, 711, 284
Schlegel, D. J., Finkbeiner, D. P., & Davis, M. 1998, ApJ, 500, 525

Schnorr-Müller, A., Storchi-Bergmann, T., Nagar, N. M., & Ferrari, F. 2014, MNRAS, 438, 3322
Schnorr Müller, A., Storchi-Bergmann, T., Riffel, R. A., et al. 2011, MNRAS, 413, 149
Schoenmakers, R. H. M., Franx, M., & de Zeeuw, P. T. 1997, MNRAS, 292, 349
Schönell, A. J., Riffel, R. A., Storchi-Bergmann, T., & Winge, C. 2014, MNRAS, 445, 414
Sellwood, J. A. 2014, RvMP, 86, 1
Shapiro, K. L., Genzel, R., Förster Schreiber, N. M., et al. 2008, ApJ, 682, 231
Sharp, R. G., & Bland-Hawthorn, J. 2010, ApJ, 711, 818
Shields, J. C., Walcher, C. J., Böker, T., et al. 2008, ApJ, 682, 104
Shlosman, I., Begelman, M. C., & Frank, J. 1990, Natur, 345, 679
Shlosman, I., Frank, J., & Begelman, M. C. 1989, Natur, 338, 45
Shlosman, I., Peletier, R. F., & Knapen, J. H. 2000, ApJL, 535, L83
Simmons, B. D., Lintott, C., Schawinski, K., et al. 2013, MNRAS, 429, 2199
Simmons, B. D., Urry, C. M., Schawinski, K., Cardamone, C., & Glikman, E. 2012, ApJ, 761, 75
Simões Lopes, R. D., Storchi-Bergmann, T., de Fátima Saraiva, M., & Martini, P. 2007, ApJ, 655, 718
Singh, R., van de Ven, G., Jahnke, K., et al. 2013, A&A, 558, A43
Springob, C. M., Haynes, M. P., Giovanelli, R., & Kent, B. R. 2005, ApJS, 160, 149
Stasińska, G., Vale Asari, N., Cid Fernandes, R., et al. 2008, MNRAS, 391, L29
Storchi-Bergmann, T., Dors, O. L., Jr., Riffel, R. A., et al. 2007, ApJ, 670, 959
Sutherland, R. S., & Dopita, M. A. 1993, ApJS, 88, 253
Swinbank, A. M., Sobral, D., Smail, I., et al. 2012, MNRAS, 426, 935
Teuben, P. J. 1991, in Warped Disks and Inclined Rings around Galaxies, ed. S. Casertano, P. D. Sackett, & F. H. Briggs (Cambridge: Cambridge Univ. Press), 40
Theureau, G., Hanski, M. O., Coudreau, N., Hallet, N., & Martin, J.-M. 2007, A&A, 465, 71
Trachternach, C., de Blok, W. J. G., Walter, F., Brinks, E., & Kennicutt, R. C., Jr. 2008, AJ, 136, 2720
Treister, E., Schawinski, K., Urry, C. M., & Simmons, B. D. 2012, ApJL, 758, L39
Tremaine, S., Gebhardt, K., Bender, R., et al. 2002, ApJ, 574, 740
Tully, R. B. 1988, Nearby galaxies catalog (Cambridge: Cambridge Univ. Press)
Tully, R. B., & Pierce, M. J. 2000, ApJ, 533, 744
Tully, R. B., Shaya, E. J., Karachentsev, I. D., et al. 2008, ApJ, 676, 184
Tully, R. B., Shaya, E. J., & Pierce, M. J. 1992, ApJS, 80, 479
van de Ven, G., & Fathi, K. 2010, ApJ, 723, 767
van Winckel, H. 2003, ARA&A, 41, 391
Veilleux, S., & Osterbrock, D. E. 1987, ApJS, 63, 295
Veilleux, S., Shopbell, P. L., Rupke, D. S., Bland-Hawthorn, J., & Cecil, G. 2003, AJ, 126, 2185
Villforth, C., Hamann, F., Rosario, D. J., et al. 2014, MNRAS, 439, 3342
Voges, E. S., & Walterbos, R. A. M. 2006, ApJL, 644, L29
Walcher, C. J., Böker, T., Charlot, S., et al. 2006, ApJ, 649, 692
Walcher, C. J., van der Marel, R. P., McLaughlin, D., et al. 2005, ApJ, 618, 237
Weinzirl, T., Jogee, S., Conselice, C. J., et al. 2011, ApJ, 743, 87
Weinzirl, T., Jogee, S., Khochfar, S., Burkert, A., & Kormendy, J. 2009, ApJ, 696, 411
Wong, T., Blitz, L., & Bosma, A. 2004, ApJ, 605, 183
Yan, R., & Blanton, M. R. 2012, ApJ, 747, 61
Yuan, F. 2007, in ASP Conf. Ser. 373, The Central Engine of Active Galactic Nuclei, ed. L. C. Ho, & J.-W. Wang (San Francisco, CA: ASP), 95